

PROBING THE IGM WITH  $\text{Ly}\alpha$  AND 21 cm FLUCTUATIONSCAROLINE HENKA<sup>1,2</sup>, ASANTHA COORAY<sup>2</sup>, CHANG FENG<sup>2</sup><sup>1</sup> Dark Cosmology Center, Niels Bohr Institute, University of Copenhagen,  
Juliane Maries Vej 30, 2100 Copenhagen, Denmark<sup>2</sup> Department of Physics & Astronomy, University of California, Irvine, CA 92697

## ABSTRACT

We study 21 cm and  $\text{Ly}\alpha$  fluctuations, as well as  $\text{H}\alpha$ , while distinguishing for  $\text{Ly}\alpha$  between emission of galactic, diffuse and scattered IGM origin. Cross-correlation information about the state of the IGM is worked out, testing neutral versus ionized medium with different tracers in a semi-numerical simulation setup. In order to path the way for constraints on reionization history and modelling beyond power spectrum information, we explore parameter dependencies of the cross-power signal between 21 cm and  $\text{Ly}\alpha$ , which displays characteristic morphology and a turn-over from negative to positive correlation at scales of a couple  $\text{Mpc}^{-1}$ . In a proof of concept for the extraction of further information on the state of the IGM using different tracers, we demonstrate the usage of the 21 cm and  $\text{H}\alpha$  cross-correlation signal to determine the relative strength of galactic and IGM emission in  $\text{Ly}\alpha$ . We conclude by showing the detectability of the 21 cm and  $\text{Ly}\alpha$  cross-correlation signal over about one decade in scale at high S/N for upcoming probes like SKA and the proposed all-sky intensity mapping satellite SPHEREx, while also including the  $\text{Ly}\alpha$  damping tail as well as 21 cm foreground avoidance in the modelling.

*Keywords:* cosmology: theory — dark ages, reionization, first stars — diffuse radiation — intergalactic medium — large-scale structure of universe

## 1. INTRODUCTION

At the epoch of reionization the first galaxies emerge some 100 million years after the Big Bang and their radiation reionizes the then cold, neutral hydrogen that makes up for most of the intergalactic medium (IGM). Regions of ionized hydrogen increase more and more in size, until they completely overlap at the end of reionization. Constraints from the  $\text{Ly}\alpha$  forest towards quasars put the end of this epoch at about one billion years after the Big Bang, or at a redshift of  $z \approx 6$  (Fan et al. 2006; McGreer et al. 2015). The exact reionization model itself is currently very uncertain, regarding for example ionizing sources that drive it, spatial structure, and the onset of reionization. Intensity mapping of emission line fluctuations provides a powerful future avenue to test reionization models and sources, star and galaxy formation, as well as the structure and composition of the intergalactic medium at high redshifts. It enables us to test a wide range of scales, with the measurement of line fluctuation power spectra being feasible by future probes.

One prominent example is the emission of the forbidden spin flip transition of neutral hydrogen, the so-called 21 cm line. Interferometers such as the Low Fre-

quency Array (LOFAR, van Haarlem et al. (2013)) and the Murchison Widefield Array (MWA, Bowman et al. (2013)) aim for detecting the global 21 cm signal; the MWA is predicted to measure the 21 cm power spectrum over more than a decade in scale (Lidz et al. 2008; Beardsley et al. 2013). Future probes as the Hydrogen epoch of reionization Array (HERA) and the Square Kilometre Array (SKA) will be able to detect power spectra of 21 cm fluctuations at high redshifts over up to two decades in scale, mapping most of the sky, as well as constrain the timing and morphology of reionization, the properties of early galaxies, and the early sources of heating (Pritchard et al. 2015; Koopmans et al. 2015; De Boer et al. 2016). A lot of work goes into modelling and preparing these detections, using semi-numerical simulations, such as 21cmFAST (Mesinger et al. 2011) or SimFast21 (Santos et al. 2010), and hydrodynamical simulations exploring the parameter space for reionization models, see e.g. Ocvirk et al. (2016).

In addition to the 21 cm line, intensity mapping of emission lines like CO, C II, O II, N II or  $\text{H}\alpha$  is a promising tool at high redshifts, testing the nature of the IGM, of star and galaxy formation (Lidz et al. 2011; Gong et al. 2012; Serra et al. 2016). Intensity mapping of the  $\text{Ly}\alpha$  line, a tracer for the ionized medium, has been

explored and modelled for high redshifts in [Silva et al. \(2013\)](#); [Pullen et al. \(2014\)](#). But not only intensity mapping at higher redshifts will prove to be important, also at lower redshifts the mapping of lines like CO and C II provides a wealth of information about the galactic and intergalactic medium. Low-redshift intensity mapping will be able to disentangle foregrounds for high-redshift measurements via cross-correlation of different tracers ([Comaschi et al. 2016](#)).

When constraining reionization, cross-correlation of different tracers, i.e., emission lines tracing the neutral versus ionized medium, provide important additional information. For example as shown in [Hutter et al. \(2016\)](#), coupling N-body/SPH simulations ([Springel et al. 2001](#); [Springel 2005](#)) with radiative transfer code ([Partl et al. 2011](#)), a negative cross-correlation shows up when cross-correlating 21 cm and Ly $\alpha$  fluctuations, that breaks parameter degeneracies present in reionization models for power spectra alone. Also, the cross-correlation of 21 cm emission and Ly $\alpha$  emitters improves constraints on the mean ionized fraction ([Sobacchi et al. 2016](#)). Encouragingly, the measurement of line fluctuations beyond 21 cm will be feasible with future missions, as for example the all-sky infrared intensity mapping satellite SPHEREx proposed in [Doré et al. \(2014\)](#) to measure emission line fluctuations.

In this paper we want to show how robust information on reionization is obtained beyond the power spectrum, when cross-correlating intensity maps of line emission for tracers of galactic emission and of neutral and ionized medium. The cross-correlation signal of intensity maps is less prone to suffer from systematics or incomplete foreground removal and is quite independent of the exact modelling of line emitting galaxies. We therefore explore in detail, including a wealth of physical effects in the simulations, the cross-correlation signal for 21 cm (tracer of neutral IGM) versus Ly $\alpha$  (tracer of ionized medium), as well as Ly $\alpha$  versus H $\alpha$  (tracer of galactic emission). We demonstrate the measurability of the cross-correlation signal, which is highly sensitive to the structure of ionized versus neutral medium and therefore crucial in constraining reionization history and models.

Our paper is organised as follows. We start with a detailed discussion of our simulation of intensity maps for 21 cm fluctuations, for different Ly $\alpha$  emission components and for H $\alpha$  emission, and show the respective power spectra in Section 2. In Section 3 we present the cross-correlation signals of 21 cm and Ly $\alpha$ , as well as Ly $\alpha$  and H $\alpha$ , and vary some of the model parameters. We conclude with signal-to-noise calculations for both 21 cm and Ly $\alpha$  auto spectra as well as their cross-power spectra for a combined measurement with SKA stage one and SPHEREx in Section 4.

## 2. SIMULATION OF LINE FLUCTUATIONS

### 2.1. 21 cm fluctuations

In this section we briefly review the simulated 21 cm line emission, which traces the neutral intergalactic medium, and will be used for cross-correlation studies in later sections. Semi-numerical codes efficiently simulate ionization and 21 cm temperature maps, while showing good agreement with both N-body/radiative transfer codes, as well as analytical modelling at redshifts relevant for the epoch of reionization ([Trac et al. 2008](#); [Santos et al. 2008](#)). With 21 cm temperature we mean the brightness temperature for the forbidden spin flip transition of neutral hydrogen in its ground state. We aim at relatively time efficient exploration of model parameter space, especially when coupling the simulation of 21 cm and Ly $\alpha$  fluctuations for cross-correlations studies, while modelling relevant effects as physical as possible and improving the modelling with parametrizations from observations. For the simulation of galactic Ly $\alpha$  and H $\alpha$  emission contributions in later sections we also want to create halo catalogues beyond perturbed Lagrangian density fields. We therefore use the parent code to 21cmFAST, DexM ([Mesinger & Furlanetto 2007](#))<sup>1</sup>, to create linear density, linear velocity, as well as evolved velocity fields at first order Lagrangian perturbation theory (Zel'dovich approximation, [Zel'dovich \(1970\)](#)) and ionization fields in the framework of an excursion set approach, while having a halo finder option to create a corresponding halo catalogue. With density, velocity, and ionization fields, the 21 cm brightness temperature offset  $\delta T_b$  of the spin gas temperature  $T_S$  from CMB temperature  $T_\gamma$  at redshift  $z$  is obtained via

$$\begin{aligned} \delta T_b(z) &= \frac{T_S - T_\gamma}{1 + z} (1 - e^{-\tau_{\nu_0}}) \\ &\approx 27 x_{HI} (1 + \delta_{nl}) \left( \frac{H}{dv_r/dr + H} \right) \left( 1 - \frac{T_\gamma}{T_S} \right) \\ &\times \left( \frac{1 + z}{10} \frac{0.15}{\Omega_m h^2} \right) \left( \frac{\Omega_b h^2}{0.023} \right) mK, \end{aligned} \quad (1)$$

where redshift is related to observed frequency  $\nu$  as  $z = \nu_0/\nu - 1$ , optical depth  $\tau_{\nu_0}$  at rest frame frequency  $\nu_0$ , ionization fraction  $x_{HI}$ , non-linear density contrast  $\delta_{nl} = \rho/\bar{\rho}_0 - 1$ , Hubble parameter  $H(z)$ , comoving gradient of line of sight velocity  $dv_r/dr$ , as well as present-day matter density  $\Omega_m$ , present-day baryonic density  $\Omega_b$ , and hubble factor  $h$ . The approximation in equation (1) assumes the post-heating regime with the CMB background temperature being much smaller than the spin gas temperature  $T_\gamma \ll T_S$ , so that the full spin gas temperature evolution with redshift can be neglected

<sup>1</sup> <http://homepage.sns.it/mesinger/Download.html>

when calculating the brightness temperature offset  $\delta T_b$ . For simulation results shown in this study we nevertheless ran the full spin temperature evolution from redshift  $z = 35$  down to  $z = 6$ , albeit more computationally costly, for consistency with the calculations of Ly $\alpha$  intensity fluctuations in the IGM in Section 2.2.2 and 2.2.3, where the full gas temperature evolution is required. Throughout this paper our fiducial cosmology assumes  $\Lambda$ CDM with parameters

$$w = -1, \Omega_m = 0.32, \Omega_K = 0, \Omega_b = 0.049, \\ h = 0.67, \sigma_8 = 0.83, n_s = 0.96, \Omega_r = 8.6 \times 10^{-5},$$

as well as  $N_{eff} = 3.046$  and  $Y_{He} = 0.24$ . Reionization model parameters are ionizing photon mean free path  $R_{mfp}^{UV}$ , minimal virial temperature of halos contributing ionising photons  $T_{vir}$ , efficiency parameter for the number of X-ray photons per solar mass of stars  $\zeta_x$ , the fraction of baryons converted to stars  $f_*$ , and the efficiency factor for ionized bubbles  $\zeta$ . A bubble of radius  $R$  is set to be ionized, when the collapse fraction smoothed on scale  $R$  fulfils the criterium  $f_{coll} \geq \zeta^{-1}$ . The fiducial reionization model parameters used throughout this paper, unless stated otherwise, are

$$R_{mfp}^{UV} = 40 \text{ Mpc}, T_{vir} = 10^4 \text{ K}, \\ \zeta_x = 10^{56}, f_* = 0.1, \zeta = 10.$$

All distances and scales are expressed in physical units, not in units of  $h^{-1}$  in the following.

Figure 1 shows the simulated density field (top panels) and 21 cm brightness temperature offset (middle panels) in a simulation box slice of (200 x 200) Mpc at redshift  $z = 10$  for mean neutral fraction  $\bar{x}_{HI} = 0.87$  (left panels) and at  $z = 7$  for  $\bar{x}_{HI} = 0.27$  (right panels). Going from  $z = 10$  to  $z = 7$ , i.e., from high to low redshift, a more peaked density field is obvious, as well as the growth of ionized patches with negligible 21 cm emission, as 21 cm emission is tracing neutral hydrogen. The two bottom panels show for comparison the corresponding simulation box of total Ly $\alpha$  surface brightness for the same density field; the simulation of Ly $\alpha$  emission is discussed in detail in Section 2.2.

We calculate temperature fluctuations on the grid  $\delta_{21}(\mathbf{x}, \mathbf{z})$  as

$$\delta_{21}(\mathbf{x}, \mathbf{z}) = \frac{\delta T_b(\mathbf{x}, \mathbf{z})}{\bar{T}_{21}(z)} - 1 \quad (2)$$

with average temperature  $\bar{T}_{21}(z)$ ; analogous for fluctuations in surface brightness. In the following we define the dimensionless 21 cm power spectrum as  $\tilde{\Delta}_{21}(k) = k^3 / (2\pi^2 V) \langle |\delta_{21}|^2 \rangle_k$  and display the dimensional power spectrum as  $\Delta_{21}(k) = \bar{T}_{21}^2 \tilde{\Delta}_{21}(k)$ .

## 2.2. Ly $\alpha$ fluctuations

The simulation of Ly $\alpha$  fluctuations during reionization for both the galactic contribution and the emission stemming from the intergalactic medium (IGM) is described in this section. By galactic component we mean the contribution coming from within the virial radius of Ly $\alpha$  emitting galaxies (LAE) themselves; the IGM component comprises both the Ly $\alpha$  background caused by X-ray/UV heating and scattering of Lyman-n photons, as well as the diffuse ionized IGM around galaxies where hydrogen recombines. Ly $\alpha$  emission itself is the transition of the electron in neutral hydrogen to the lowest energy state  $n = 1$  from  $n = 2$ .

### 2.2.1. Parametrizing Ly $\alpha$ luminosities

We start by describing our procedure for modelling the Ly $\alpha$  emission from galaxies. The different contributions for Ly $\alpha$  emission from galaxies are closely related with star formation and therefore can be connected to the star formation rate (SFR) of galaxies as a function of redshift and halo mass. Dominant source for Ly $\alpha$  galactic emission is mainly hydrogen recombination, as well as collisional excitation. Two more subdominant contributors to galactic Ly $\alpha$  emission are continuum emission via stellar, free-free, free-bound and two photon emission, as well as gas cooling via collisions and excitations in gas of temperatures smaller than  $T_K \approx 10^4 \text{ K}$  (Fardal et al. 2001; Guo et al. 2011; Dopita et al. 2003; Fernandez & Komatsu 2006).

We start with recombination as a source of galactic Ly $\alpha$  emission. Ionizing equilibrium in the interstellar gas is assumed, so that a fraction  $f_{rec} \approx 66\%$  of hydrogen recombinations result in the emission of one Ly $\alpha$  photon, for spherical clouds of about  $10^4 \text{ K}$  (Gould & Weinberg 1996). The fraction of Ly $\alpha$  photons not absorbed by dust is parametrized as in Hayes et al. (2011)

$$f_{Lya}(z) = C_{dust} 10^{-3} (1+z)^\zeta, \quad (3)$$

with  $C_{dust} = 3.34$  and  $\zeta = 2.57$ . Following simulations the escape fraction of ionizing photons can be fitted by

$$f_{esc}(z) = \exp \left[ -\alpha(z) M^{\beta(z)} \right], \quad (4)$$

with halo mass  $M$  as well as  $\alpha$  and  $\beta$  parametrized as functions of redshift as in Razoumov & Sommer-Larsen (2010). The number of Ly $\alpha$  photons emitted in a galaxy per second can then be expressed as

$$\dot{N}_{Lya} = A_{He} f_{rec} f_{Lya} (1 - f_{esc}) \dot{N}_{ion}, \quad (5)$$

with the photon fraction that goes into helium ionization  $A_{He} = (4 - Y_p) / (4 - 3Y_p)$ , with helium mass fraction  $Y_p$ , and the rate of ionizing photons emitted by stars  $\dot{N}_{ion} = Q_{ion} \times \text{SFR}$ . The average number of ionizing photons emitted per solar mass of star formation is taken



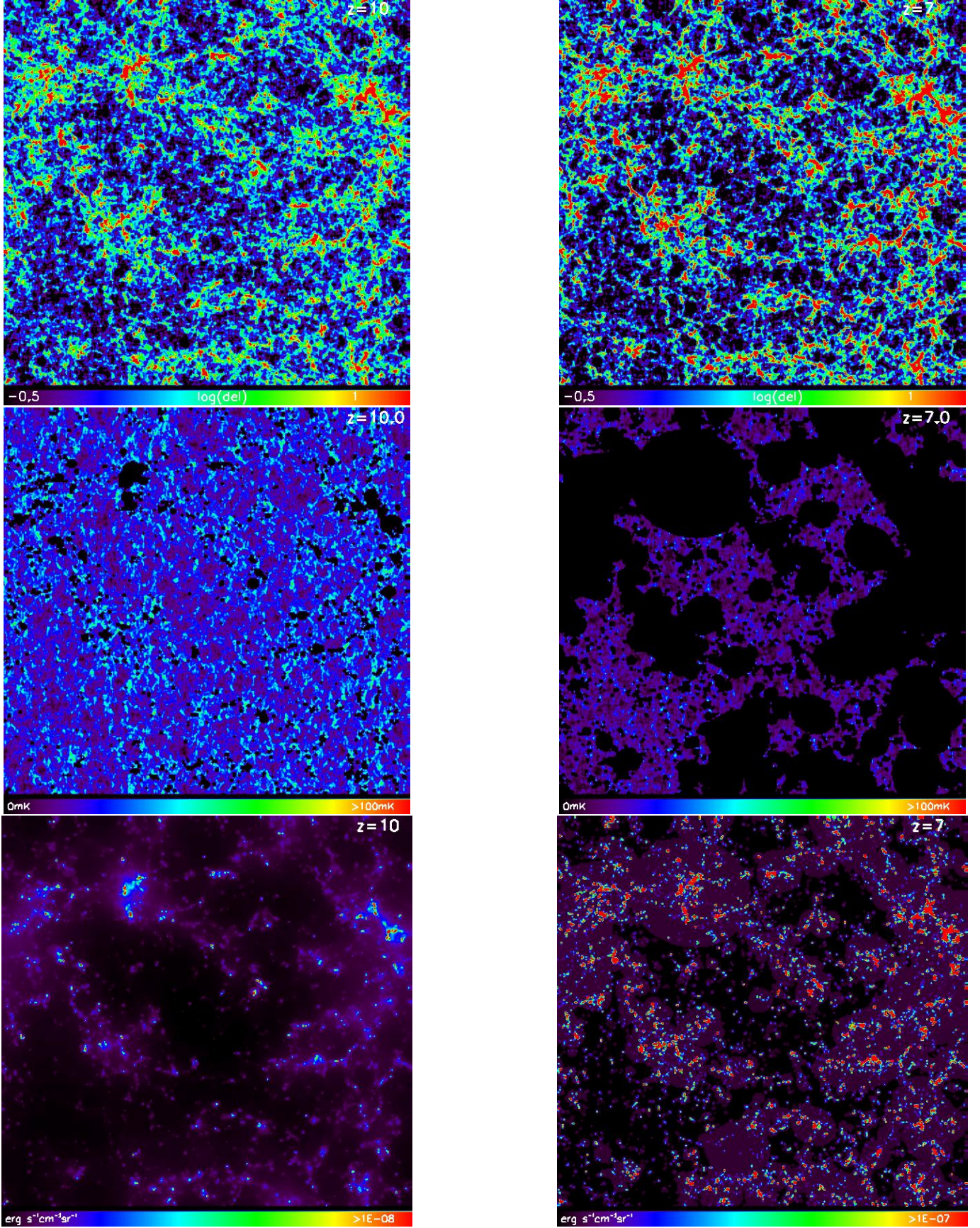


**Figure 1.** Slices of simulated density (top) and corresponding 21 cm brightness temperature offset  $\delta T_b$  (middle) in a 200 Mpc box. Left: redshift  $z = 10$  and mean neutral fraction of  $\bar{x}_{HI} = 0.87$ ; Right: redshift  $z = 7$  and  $\bar{x}_{HI} = 0.27$ ; parameter settings as in Section 2.1. The two bottom panels show for comparison the total simulated Ly $\alpha$  surface brightness in  $\text{erg s}^{-1}\text{cm}^{-2}\text{sr}^{-1}$ ; for a detailed descriptions of these simulations, and a description of different contributions to Ly $\alpha$  emission taken into account, see Section 2.2.



to be  $Q_{ion} \approx 6 \times 10^{60} M_{\odot}^{-1}$ , following the parametrization of stellar lifetime and number of ionizing photons emitted per unit time for population II star spectral energy distributions (SED) of solar metallicity in [Schaerer \(2002\)](#) and integrating over a Salpeter initial mass function. The galactic component of Ly $\alpha$  luminosity due to recombination is then simply given by

$$L_{rec}^{gal} = E_{Ly\alpha} \dot{N}_{Ly\alpha}, \quad (6)$$

where we assume emission at the Ly $\alpha$  rest frequency  $\nu_0 = 2.47 \times 10^{15}$  Hz at energy  $E_{Ly\alpha} = 1.637 \times 10^{-11}$  erg.

The Ly $\alpha$  emission from excitation during hydrogen ionization is estimated in [Silva et al. \(2013\)](#) for thermal equilibrium, taking SED results from [Maraston \(2005\)](#) to get an average ionizing photon energy of  $E_{\nu} = 21.4$  eV, which relates to the energy emitted as Ly $\alpha$  radiation due to collisional excitation as  $E_{exc}/E_{\nu} \approx 0.1$  ([Gould & Weinberg 1996](#)). The Ly $\alpha$  luminosity from excitations of the interstellar medium then reads

$$L_{exc}^{gal} = f_{Ly\alpha} (1 - f_{esc}) A_{He} E_{exc} \dot{N}_{ion}, \quad (7)$$

again as in the recombination case depending on the parametrization of the SFR as a function of mass and redshift via the rate of ionizing photons  $\dot{N}_{ion}$ .

The crucial relation between star formation rate and halo mass for the calculation of Ly $\alpha$  luminosities is parametrized to match the observed trend of an increased SFR for smaller mass halos, becoming almost constant for larger halo masses with  $M > 10^{11} M_{\odot}$  ([Conroy & Wechsler 2009](#); [Popesso et al. 2012](#)). The parametrization we use throughout this paper is taken from [Silva et al. \(2013\)](#) and was obtained by fitting to a reasonable reionization history, together with a Ly $\alpha$  luminosity function compatible with observations. This SFR reads

$$\frac{\text{SFR}}{M_{\odot}/\text{yr}} = (2.8 \times 10^{-28}) M^a \left(1 + \frac{M}{c_1}\right)^b \left(1 + \frac{M}{c_2}\right)^d, \quad (8)$$

with fitting parameters  $a = -0.94$ ,  $d = -1.7$ ,  $c_1 = 10^9 M_{\odot}$ , and  $c_2 = 7 \times 10^{10} M_{\odot}$ . Plugging this SFR into Ly $\alpha$  luminosities equation (6) gives the dependency of Ly $\alpha$  luminosity on halo mass at fixed redshift. The redshift evolution of Ly $\alpha$  galactic emission depends on escape fraction  $f_{esc}(z)$ , fraction of Lyman-photons not absorbed by dust  $f_{Ly\alpha}(z)$ , as well as halo number, mass, and distribution (also creating a spatial distribution of galactic luminosities). The total galactic Ly $\alpha$  luminosity due to recombination and excitation is given by

$$L^{gal}(M, z) = L_{rec}^{gal}(M, z) + L_{exc}^{gal}(M, z), \quad (9)$$

for each halo of mass  $M$  at redshift  $z$ . For simulation boxes with each voxel defined by position  $\mathbf{x}$  and redshift  $z$ , one can sum the luminosities per voxel and divide by

the comoving voxel volume, in order to get a smoothed luminosity density (per comoving volume) on the grid  $l^{gal}(\mathbf{x}, z)$ . For the luminosities per voxel we smoothed the Ly $\alpha$  emission over virial radii before. The comoving luminosity density then can easily be converted to surface brightness  $I_{\nu}^{gal}(\mathbf{x}, z)$  via

$$I_{\nu}^{gal}(\mathbf{x}, z) = y(z) d_A^2(z) \frac{l^{gal}(\mathbf{x}, z)}{4\pi d_L^2}, \quad (10)$$

with comoving angular diameter distance  $d_A$ , proper luminosity distance  $d_L$ , and  $y(z) = d\chi/d\nu = \lambda_0(1+z)^2/H(z)$  (for comoving distance  $\chi$ , observed frequency  $\nu$  and rest-frame wavelength  $\lambda_0 = 2.46 \times 10^{-15}$  m of Ly $\alpha$  radiation). By assigning Ly $\alpha$  luminosities to host halos depending on halo masses, we have created a spatial distribution of galactic luminosities in our simulation that follows the halo distribution and therefore naturally is position-dependent, as can clearly be seen in Figure 2 (top panels). Here we show the Ly $\alpha$  surface brightness for the direct galactic emission component  $I_{\nu}^{gal}(\mathbf{x}, z)$  in slices through our simulation, box length 200 Mpc, at redshift  $z = 10$  (left) and  $z = 7$  (right), with more halos lighting up in Ly $\alpha$  while reionization progresses.

### 2.2.2. Ly $\alpha$ emission from the diffuse IGM

In addition to direct galactic emission, the Ly $\alpha$  emission region is also comprised of the ionized diffuse IGM around halos ([Pullen et al. 2014](#)). Here ionizing radiation escapes the halos of Ly $\alpha$  emitting galaxies and can ionize neutral hydrogen in the diffuse IGM. Similar to the emission from within halos, Ly $\alpha$  radiation is then re-emitted through recombinations. The comoving number density of recombinations in the diffuse IGM reads

$$\dot{n}_{rec}(\mathbf{x}, z) = \alpha_A n_e(z) n_{HII}(z), \quad (11)$$

with the case A recombination coefficient  $\alpha_A$  for moderately high redshifts, free electron density  $n_e = x_i n_b$  (depending on ionization fraction  $x_i$  and baryonic comoving number density  $n_b$ ), and with  $n_{HII} = x_i n_b (4 - 4Y_p) / (4 - 3Y_p)$ , the comoving number density of ionized hydrogen ( $Y_p$  is the helium mass fraction). The comoving recombination coefficient  $\alpha_A$  depends on the IGM gas temperature  $T_K$  via ([Abel et al. 1997](#); [Furlanetto et al. 2006](#))

$$\alpha_A \approx 4.2 \times 10^{-13} (T_K/10^4 \text{K})^{-0.7} (1+z)^3 \text{cm}^3 \text{s}^{-1}. \quad (12)$$

The Ly $\alpha$  luminosity density due to recombinations in the IGM is given by

$$l_{rec}^{IGM}(\mathbf{x}, z) = f_{rec} \dot{n}_{rec}(\mathbf{x}, z) E_{Ly\alpha}, \quad (13)$$

where we insert for the fraction of Ly $\alpha$  photons emitted per hydrogen recombination  $f_{rec} \approx 0.66$  as in Section 2.2.1 for the galactic contribution and a Ly $\alpha$  rest

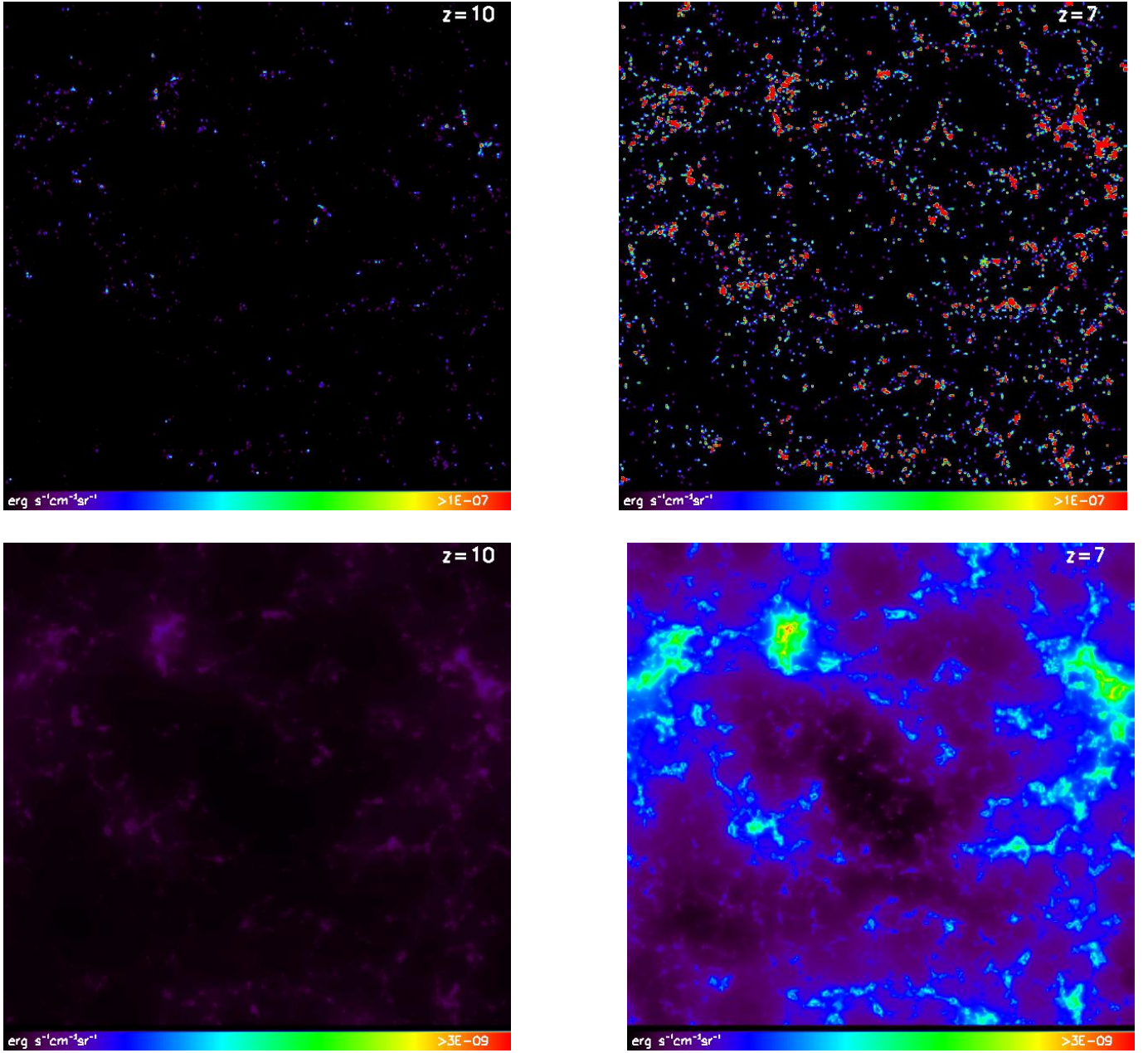


**Figure 2.** Slices of simulations of Ly $\alpha$  surface brightness in  $\text{erg s}^{-1} \text{cm}^{-2} \text{sr}^{-1}$  at  $(z = 10, \bar{x}_{HI} = 0.87)$  (left) and  $(z = 7, \bar{x}_{HI} = 0.27)$  (right), 200Mpc box length; Top: Galactic Ly $\alpha$  emission  $\nu I_{\nu}^{gal}(\mathbf{x}, z)$  as described in Section 2.2.1; Bottom: Scattered IGM component  $\nu I_{\nu}^{sIGM}(\mathbf{x}, z)$  as described in Section 2.2.3.

frame energy of  $E_{Ly\alpha} = 1.637 \times 10^{-11} \text{erg}$ .

We simulate the number density of recombinations per pixel by evolving gas temperature  $T_K$ , baryonic comoving number density  $n_b$ , and ionization fraction  $x_i$  in the IGM and by calculating the Ly $\alpha$  luminosity density for each pixel in our simulation box. The baryonic comoving number density  $n_b(\mathbf{x}, z)$  is calculated making use of the non-linear density contrast generated by the DexM code (Mesinger & Furlanetto 2007), see also Section 2.1, via  $n_b(\mathbf{x}, z) = \bar{n}_b (1+z)^3 [1 + \delta_{nl}(\mathbf{x}, z)]$ , where we take the present-day mean baryonic number

density as  $\bar{n}_b(\mathbf{x}, z) = 1.905 \times 10^{-7} \text{cm}^{-3}$ . When evolving gas temperature fluctuations, we extract the gas temperature  $T_K(\mathbf{x}, z)$  from the evolution equations for the full spin temperature evolution in the DexM code, which keeps track of the inhomogeneous heating history of the gas. Alternatively, we can make a conservative estimate for Ly $\alpha$  brightness fluctuations by neglecting fluctuations in gas temperature  $T_K$  and in baryonic density  $n_b$ . When ignoring density perturbations we can set the comoving baryonic number density to  $\bar{n}_b(z) = 1.905 \times 10^{-7} (1+z)^3 \text{cm}^{-3}$ . For the case of con-

stant gas temperature in halos we choose  $T_K = 10^4$  K, corresponding to typical halo virial temperatures.

The luminosity density  $l_{rec}^{IGM}(\mathbf{x}, z)$  can easily be converted into surface brightness  $I_{\nu, rec}^{IGM}(\mathbf{x}, z)$  of the diffuse IGM via

$$I_{\nu, rec}^{IGM}(\mathbf{x}, z) = y(z) d_A^2(z) \frac{l_{rec}^{IGM}(\mathbf{x}, z)}{4\pi d_L^2}, \quad (14)$$

as was done in equation (10) for the galactic contribution to the total Ly $\alpha$  surface brightness.

In Figure 3 we compare simulations of the Ly $\alpha$  surface brightness for the diffuse IGM component when making a conservative estimate of the brightness fluctuations by neglecting fluctuations in gas temperature  $T_K$  and in comoving baryonic density  $n_b$  (top panels), when taking into account fluctuations in gas temperature  $T_K$  (middle panels), and when taking into account fluctuations in both gas temperature  $T_K$  and comoving baryonic density  $n_b$  (bottom panels), for the case of redshift  $z = 10$  (left panels) and  $z = 7$  (right panels). As expected, fluctuations in surface brightness become more pronounced when taking into account fluctuations in gas temperature and baryonic density.

### 2.2.3. Ly $\alpha$ emission from the scattered IGM

In this section we briefly describe the scattered IGM background in Ly $\alpha$  during reionization. Main contributors are X-ray and UV heating, as well as direct stellar emission via scattering in the IGM of Lyman-n photons emitted from galaxies. Unlike the galactic contribution in Section 2.2.1, where the parametrization boils down to a dependence on halo mass via the SFR, for the scattered IGM emission in Ly $\alpha$  we need to follow the evolution of gas temperature and ionization state at each point  $(\mathbf{x}, z)$  in the simulation box, as done for the diffuse IGM in the previous section. We make use of the Ly $\alpha$  background evolved as described in Mesinger et al. (2011) for 21cmFAST/DexM. It takes into account X-ray excitation of neutral hydrogen, with X-ray heating balanced by photons redshifting out of Ly $\alpha$  resonance (Pritchard & Furlanetto 2007), as well as direct stellar emission of photons in the UV emitted between the Ly $\alpha$  frequency and the Lyman limit that redshift into Lyman-n resonance and are absorbed by the IGM. The emission due to stellar emissivity is estimated as a sum over Lyman resonances as e.g. in (Barkana & Loeb 2005). Snapshots of the spherically averaged Ly $\alpha$  photon counts per unit area, unit time, unit frequency, and unit steradian  $J_\alpha$  due to X-ray heating and direct stellar emission in the UV are extracted and converted to Ly $\alpha$  surface brightness of the scattered IGM  $I_\nu^{sIGM}(\mathbf{x}, z)$  via (Silva et al. 2013)

$$I_\nu^{sIGM}(\mathbf{x}, z) = \frac{6E_{Ly\alpha} d_A^2}{(1+z)^2 d_L^2} J_\alpha. \quad (15)$$

We note, that in the setup used here, the Ly $\alpha$  background does not include soft-UV sources as for example quasars. It is also important to mention that the same density fields, and therefore ionization and halo fields derived, are used for both the diffuse and scattered IGM components shown, alongside with the galactic emission in Ly $\alpha$ . Figure 2 (bottom panels) shows the extracted IGM component in Ly $\alpha$  surface brightness at  $z = 10$  and  $z = 7$ . Between  $z = 10$  and  $z = 7$  the scattered IGM is clearly lit up in Ly $\alpha$  intensity, with filamentary structures more pronounced at lower redshift.

### 2.2.4. Power spectra and summary Ly $\alpha$ simulation

Steps taken to simulate Ly $\alpha$  surface brightness fluctuations are summed up in the following.

After parametrizing the Ly $\alpha$  luminosities as a function of redshift and halo mass in Section 2.2.1, we need to assign luminosities to host halos. We run a halo finder on the density field at a given redshift, evolved from one set of initial density fluctuations. Then luminosities are assigned to galaxy host halos with halo masses above a minimum mass  $M_{min}$  (corresponding for example to  $M_{min} = 1.3 \times 10^8 M_\odot$  at  $z = 7$ ), equivalent to a minimum virial temperature  $T_{vir} = 10^4$  K needed for sufficient efficiency of baryonic cooling when forming galaxies. Maximum halo masses found correspond to  $\approx 3 \times 10^{11} M_\odot$  at  $z = 10$  and  $\approx 2 \times 10^{12} M_\odot$  at  $z = 7$ . As mentioned in Section 2.2.1, equation (8) is a parametrization of the star formation rate that captures a reionization history and luminosity function compatible with observations, fitting the abundance of Ly $\alpha$  emitters. A possible further tuning of the simulated luminosities to an observed luminosity function can be obtained in this step by varying the duty cycle  $f_{duty}$ , which randomly switches on  $f_{duty}$ -percent of halos as hosting a galaxy. A duty cycle  $f_{duty} = 1$  means that all halos above  $M_{min}$  are assumed to host a galaxy that emits in Ly $\alpha$ ; a duty cycle smaller than one takes into account that not all halos might host a galaxy bright in Ly $\alpha$ . We set  $f_{duty}$  to one here, as our SFR was tuned to fit luminosity functions from observations, but will briefly show the impact of introducing a duty cycle smaller than one in Section 3.1.2. Also to take into account a distribution of satellite galaxies can be used to further refine the distribution of Ly $\alpha$  emitters in future analyses. After assigning Ly $\alpha$  luminosities to host halos, we build the smoothed field of the galactic contribution  $I_\nu^{gal}(\mathbf{x}, z)$  to Ly $\alpha$  surface brightness as in equation (10); shown in Figure 2 (top panels) for redshift  $z = 10$  (left) and  $z = 7$  (right).

In addition to the surface brightness due to direct galactic emission, the emitting region is also comprised of ionized diffuse IGM around halos as discussed in Section 2.2.2. The resulting Ly $\alpha$  surface brightness



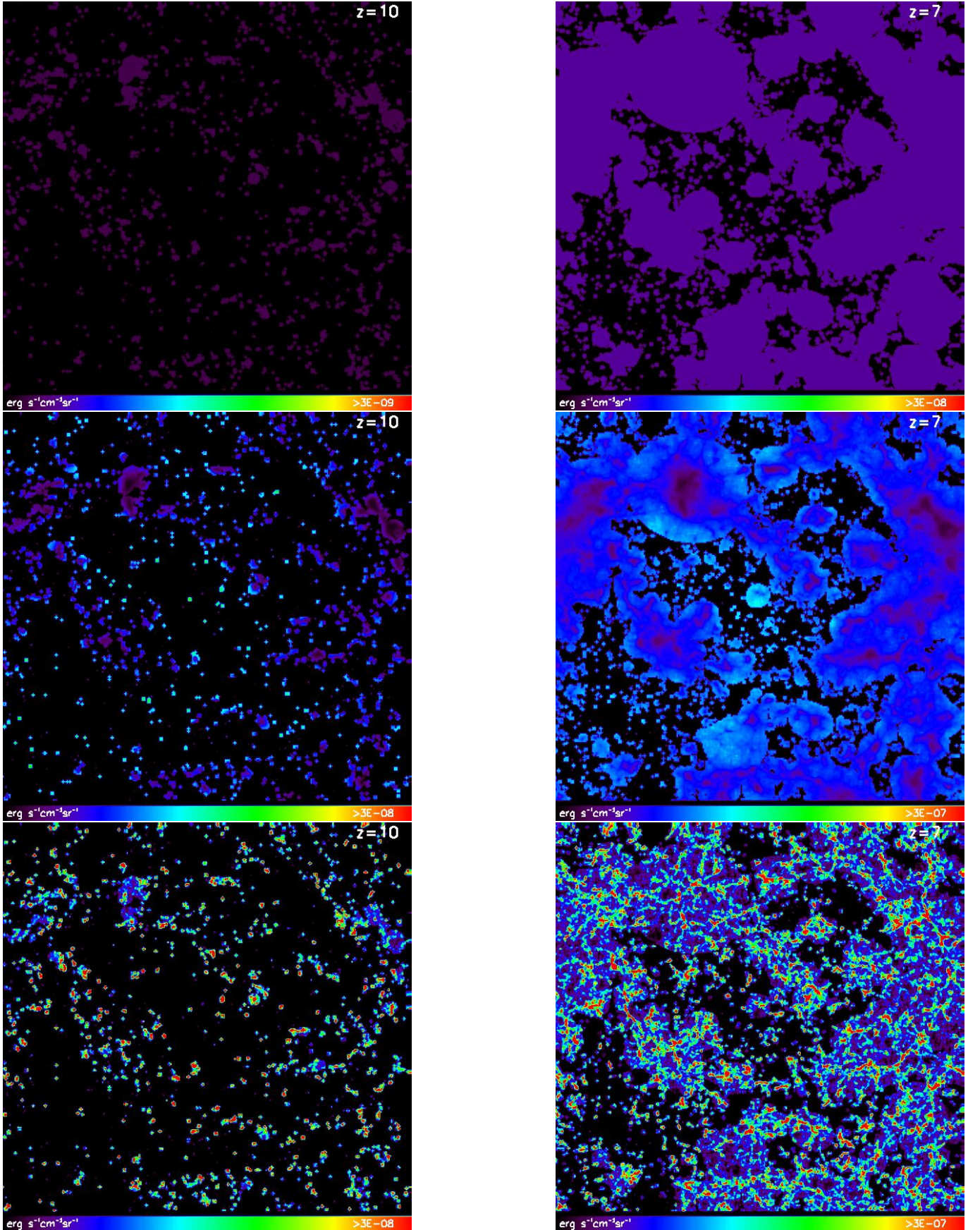


**Figure 3.** Slices of simulations of 200 Mpc box length at ( $z = 10$ ,  $\bar{x}_{HI} = 0.87$ ) (left) and ( $z = 7$ ,  $\bar{x}_{HI} = 0.27$ ) (right) of Ly $\alpha$  surface brightness in  $\text{erg s}^{-1} \text{cm}^{-2} \text{sr}^{-1}$  for the diffuse IGM  $I_{\nu, \text{rec}}^{IGM}(\mathbf{x}, z)$ . Top panels depict the brightness fluctuations for constant gas temperature and comoving baryonic density, middle panels for varying gas temperature and constant comoving baryonic density, and bottom panels for both gas temperature and comoving baryonic density varying.



$I_{\nu,rec}^{IGM}(\mathbf{x}, z)$  is given by equation (14) and presented in Figure 3 for redshift  $z = 10$  (left panels) and  $z = 7$  (right panels), when neglecting fluctuations in gas temperature and comoving baryonic density (top panels), when taking into account fluctuations in gas temperature  $T_K$  (middle panels), and in both gas temperature  $T_K$  and comoving baryonic density  $n_b$  (bottom panels). Alongside with the modelling of galactic emission from the halo and emission from the surrounding diffuse IGM, we run the evolution of the scattered Ly $\alpha$  background for the same density, ionization field, and halo fields, taking into account UV/X-ray heating and scattering of Lyman-n photons. We therefore only treat one realization of density, luminosity, and brightness fields. The UV/X-ray heating and scattering of Lyman-n photons gives the scattered IGM contribution to the Ly $\alpha$  surface brightness  $I_{\nu,diff}^{IGM}(\mathbf{x}, z)$ , as described in Section 2.2.3 and shown in Figure 2 (bottom panels) for redshift  $z = 10$  (left) and  $z = 7$  (right). For the simulation of both emission from the scattered and the diffuse IGM, we run the full evolution of gas temperature and gas density, as well as ionization fraction of the IGM.

Having simulated the different contributions to Ly $\alpha$  surface brightness, the fluctuations in the smoothed surface brightness field read

$$\delta_{I_\nu}(\mathbf{x}, z) = \sum_i \frac{\nu I_{\nu,i}(\mathbf{x}, z)}{\nu \bar{I}_{\nu,i}(z)} - 1, \quad (16)$$

summing, when wanted, pixelwise at observed frequency  $\nu$ , over Ly $\alpha$  contributions to the surface brightness, i.e., galactic, diffuse, and scattered IGM, with mean Ly $\alpha$  surface brightness  $\bar{I}_\nu(z)$ . We display the dimensionless power spectrum as  $\tilde{\Delta}_{Ly\alpha}(k) = k^3 / (2\pi^2 V) \langle |\delta_{I_\nu}|^2 \rangle_k$  and, when a comparison of absolute emission strength is desirable, the dimensional power spectrum as  $\Delta_{Ly\alpha}(k) = (\nu \bar{I}_\nu)^2 \tilde{\Delta}_{Ly\alpha}(k)$ .

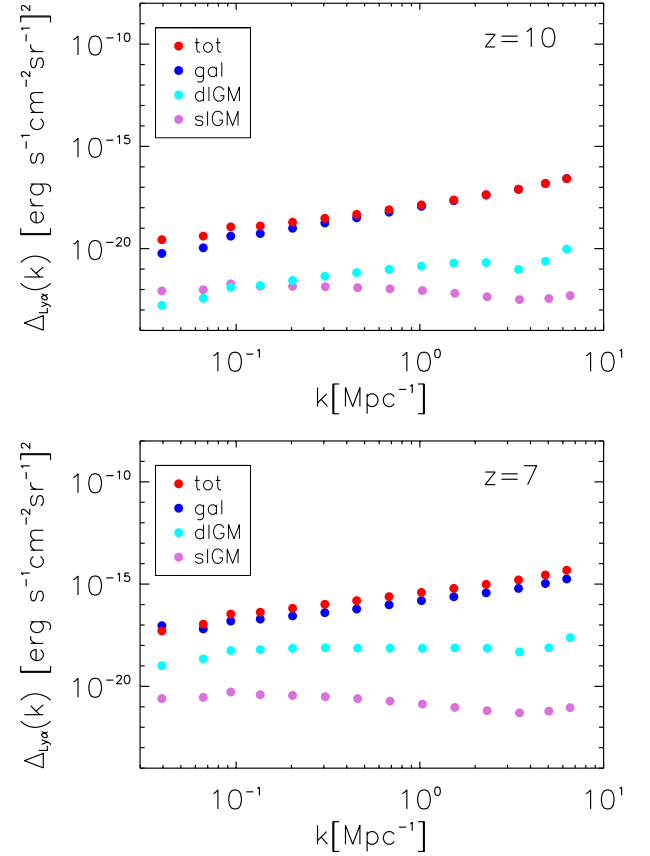
Figure 4 shows at redshift  $z = 10$  (top panel) and  $z = 7$  (bottom panel) power spectra for the three dominant contributions to Ly $\alpha$  surface brightness fluctuations, i.e., for direct galactic emission (gal), for diffuse IGM emission (dIGM), when neglecting fluctuations in gas temperature and comoving baryonic density, and for scattered IGM emission (sIGM), as well as total emission (tot). The Ly $\alpha$  surface brightness of the diffuse IGM component proves to be sub-dominant and less k-dependent as compared to the galactic emission component, and again the power increases at lower redshift towards a fully ionized universe. Table 1 sums up the corresponding mean intensities for each emission component. As a check of consistency, we compare with Ly $\alpha$  power spectrum results from other work in Appendix A.

Figure 5 depicts the power spectra of Ly $\alpha$  surface brightness for the diffuse IGM both when neglecting and when taking into account fluctuations in gas tempera-

**Table 1.** Mean surface brightness of Ly $\alpha$  emission for different sources at redshift  $z = 10$  and  $z = 7$

Source of emission (erg s <sup>-1</sup> cm <sup>-2</sup> sr <sup>-1</sup> )	$\nu I_\nu(z = 10)$	$\nu I_\nu(z = 7)$
Total	$3.1 \times 10^{-9}$	$1.8 \times 10^{-8}$
Galactic	$3.3 \times 10^{-10}$	$1.0 \times 10^{-8}$
Diffuse IGM	$2.7 \times 10^{-9}$	$5.1 \times 10^{-9}$
Scattered IGM	$2.5 \times 10^{-11}$	$2.9 \times 10^{-9}$

NOTE. - See Figure 4 for corresponding power spectra.



**Figure 4.** Ly $\alpha$  power spectra in surface brightness ( $\nu I_\nu$ ): total emission (tot, red), galaxy (gal, blue), diffuse IGM (dIGM, cyan) and scattered IGM (sIGM, orchid) contributions for redshift  $z = 10$  (top panel) and  $z = 7$  (bottom panel).

ture and comoving baryonic density for redshift  $z = 10$  (top panels) and redshift  $z = 7$  (bottom panels). As expected, taking into account temperature and density fluctuations increases the power. We will take the simulation of the Ly $\alpha$  emission in the diffuse IGM for constant gas temperature and constant baryonic density as a conservative lower bound for our cross-correlation studies in the following sections, as also our simulation of 21 cm emission deal with a uniform ionization field (each pixel is assigned to be either fully ionized or neutral).

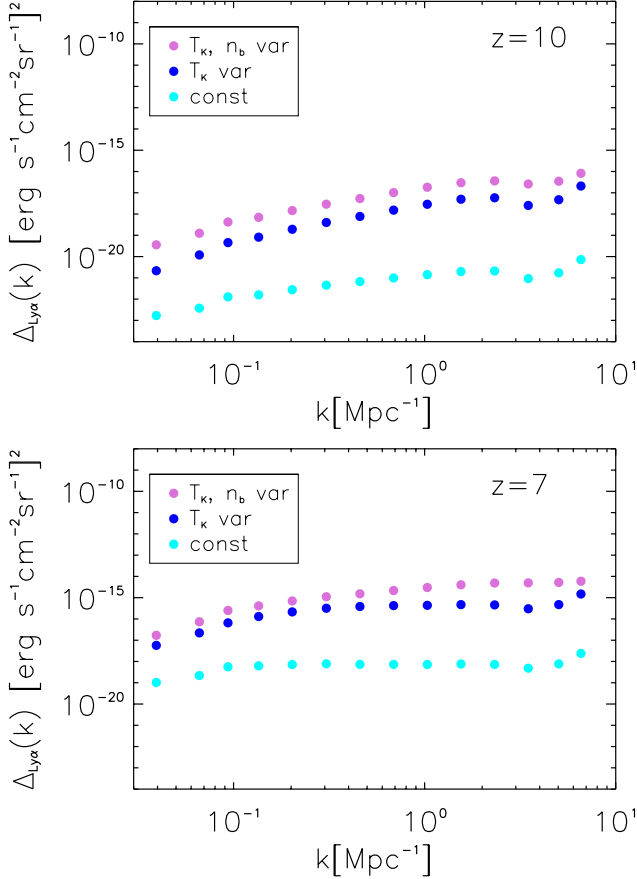


**Figure 5.** Ly $\alpha$  power spectra in surface brightness ( $\nu I_\nu$ ) for the diffuse IGM contribution: taking into account fluctuations in both gas temperature  $T_K$  and comoving baryonic density  $n_b$  (orchid, top), only fluctuations in gas temperature  $T_K$  (blue, middle), and for constant  $T_K$  and  $n_b$  (cyan, bottom), at redshift  $z = 10$  (top panel) and  $z = 7$  (bottom panel).

### 2.3. H $\alpha$ fluctuations and power spectra

Unlike Ly $\alpha$ , which also has an IGM component, both diffuse and scattered, H $\alpha$  emission can be assumed to be of purely galactic origin. It traces the ionized hydrogen component in galaxies. Thus H $\alpha$  is an interesting tracer of the galaxy-only component in emission, as compared to Ly $\alpha$ , and can be used to single out the amount of the galactic contribution versus IGM contribution in Ly $\alpha$  brightness via cross-correlation of the two tracers.

Similar to the assignment of Ly $\alpha$  luminosities depending on halo mass and redshift in Section 2.2.1, we also parametrize the H $\alpha$  luminosities to ultimately depend on halo mass and redshift. We use the relation between total star formation rate SFR and H $\alpha$  luminosity from Kennicutt (1998), that reads

$$L_{H\alpha} = 1.26 \times 10^{41} (\text{erg s}^{-1}) \times \text{SFR} (M_\odot \text{yr}^{-1}), \quad (17)$$

and assign intrinsic H $\alpha$  luminosities to host halos according to their mass. Again, as for the modelling of Ly $\alpha$  emission, we assume a minimum host halo virial

temperature of  $T_{\text{vir}} = 10^4$  K for baryonic cooling to be efficient and halos to be able to host a galaxy. For the power spectrum we calculate surface brightness fluctuations per pixel smoothed over virial radii, analogous to equation (9) for Ly $\alpha$  galactic emission. The power spectrum (for fluctuations in brightness intensity) is shown together with the distribution of luminous halos at redshift  $z = 10$  and  $z = 7$  in Figure 6. Note that the intrinsic power in H $\alpha$  is about two orders of magnitude lower than for Ly $\alpha$ , which approximately reflects the intrinsic line ratio of about 8.7 (Brookhurst 1971; Hummer & Storey 1987) between the two emission lines. We neglect for now dust obscuration of H $\alpha$  sources, as we aim in Section 3.3 at a proof of concept for singling out the IGM part of Ly $\alpha$  emission via cross-correlation with galactic H $\alpha$  emission.

## 3. CROSS-CORRELATION STUDIES

In this section we present results for the cross-correlation signal of brightness fluctuations in 21 cm, Ly $\alpha$  and H $\alpha$  emission; their simulation has been described in the previous sections. The goal is to explore robust probes beyond the power spectrum, which will enable us to probe the state of the IGM during reionization. We start with the cross-correlation signal for 21 cm and different components of Ly $\alpha$  brightness fluctuations in Section 3.1.1. We proceed to show the impact on the cross-correlation signal when varying some of the model parameters in Section 3.1.2. We finish by presenting a method to single out the IGM component in Ly $\alpha$  brightness fluctuations by cross-correlating with H $\alpha$  fluctuations in Section 3.3.

We define the dimensionless cross-power spectrum as  $\tilde{\Delta}_{I,J} = k^3 / (2\pi^2 V) \Re \langle \delta_I \delta_J^* \rangle_k$  for fluctuations  $\delta_I$  and  $\delta_J$ , as well as the dimensional cross-power spectrum as  $\Delta_{I,J}(k) = \bar{I}_I \bar{I}_J \tilde{\Delta}_{I,J}(k)$  for mean intensities  $\bar{I}_I$  and  $\bar{I}_J$ . As a measure of how correlated or anti-correlated modes are, we also display the cross-correlation coefficient  $CCC$ . It gives  $0 < CCC < 1$  for correlated modes and  $-1 < CCC < 0$  for anti-correlated modes; it is defined as

$$CCC_{I,J}(k) = \frac{\Delta_{I,J}(k)}{\sqrt{\Delta_I(k) \Delta_J(k)}}, \quad (18)$$

with power spectra  $\Delta_I$  and  $\Delta_J$  of fluctuations  $\delta_I$  and  $\delta_J$ , and the cross-power spectrum  $\Delta_{I,J}$ .

### 3.1. 21 cm and Ly $\alpha$ fluctuations

#### 3.1.1. Galactic, diffuse IGM and scattered IGM

The cross-correlation between fluctuations in 21 cm and Ly $\alpha$  brightness is useful to characterize the intergalactic medium (IGM), as 21 cm emission traces the neutral part of the IGM, and Ly $\alpha$  emission is more closely connected to ionized regions. Ly $\alpha$  emission is



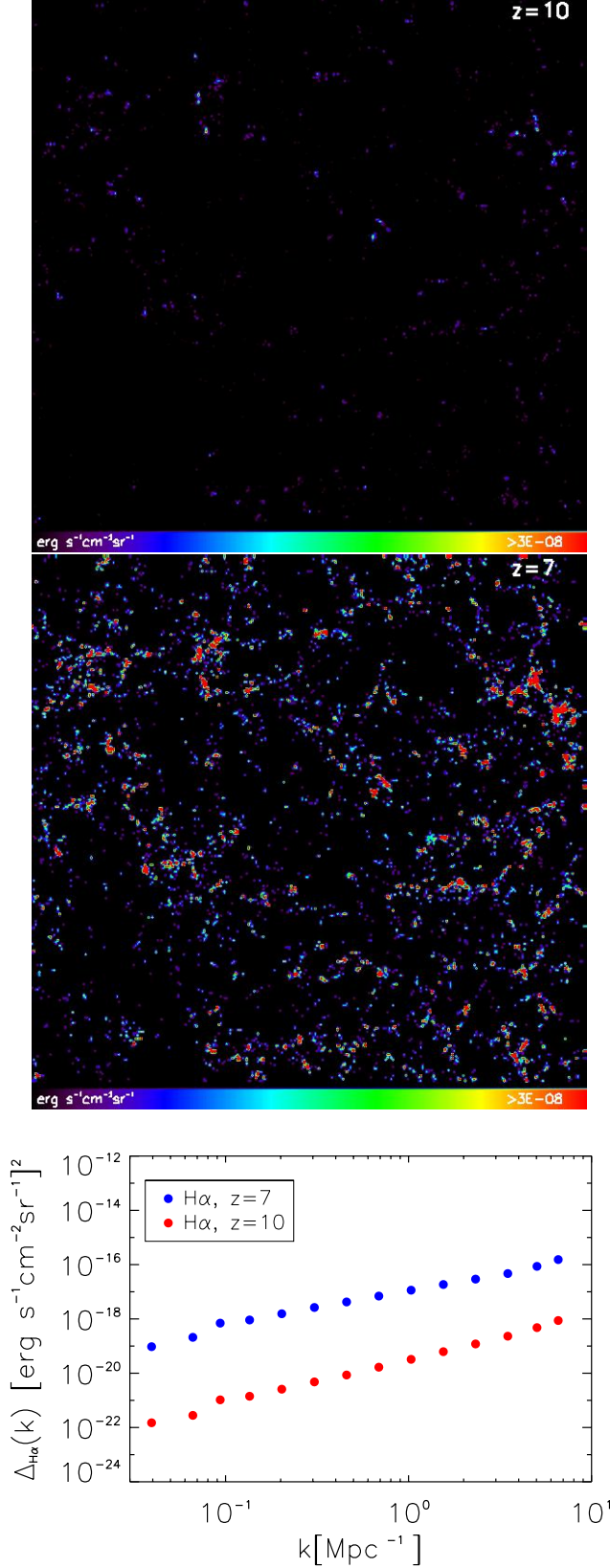


**Figure 6.** Top and middle: Simulated box slices of  $(200 \times 200)$  Mpc at  $z = 10$  (top) and  $z = 7$  (middle) of  $H\alpha$  intrinsic surface brightness (not corrected for dust absorption) in  $\text{erg s}^{-1}\text{cm}^{-2}\text{sr}^{-1}$  for luminosities assigned to host halos as in equation (17). Bottom: Corresponding power spectra at  $z = 7$  (blue, top) and  $z = 10$  (red, bottom).

made up of galactic emission and emission in the diffuse ionized IGM, plus sub-dominantly a contribution from scattering in the IGM. The cross-correlation with 21 cm emission therefore is sensitive to the clustering and size of ionized regions. An anti-correlation between 21 cm and  $\text{Ly}\alpha$  emission sensitive to the structure of the ionized medium during the epoch of reionization can be expected at large and intermediate scales; as well as a turnover to positive correlation at small scales (as both tracers follow the same underlying density field).

We cross-correlate 21 cm fluctuations simulated as described in Section 2.1 with the components of  $\text{Ly}\alpha$  fluctuations presented in Section 2.2, i.e., diffuse and scattered IGM components, and the galactic emission component. Figure 7 shows the breakdown of the dimensional cross-power spectrum (left) and the cross-correlation coefficient (CCC, right) for diffuse and scattered IGM components, as well as the galactic component of  $\text{Ly}\alpha$  fluctuations cross-correlated with 21 cm fluctuations. Going from redshift  $z = 10$  to  $z = 7$  and from a higher mean neutral fraction of  $\bar{x}_{HI} = 0.87$  to  $\bar{x}_{HI} = 0.27$ , the morphology of the cross-correlation clearly shifts to a stronger anti-correlation at small  $k$  (larger scales), with the cross-correlation signal as shown in the dimensional cross-power spectrum dominated by galactic emission, and diffuse emission gaining importance towards lower redshift. The diffuse IGM component proves to be strongly anti-correlated with a CCC close to -1, closely tracing the extended ionized medium. To check consistency of results, when taking for example at  $z = 7$  the dimensional Lyman- $\alpha$  power spectra in Figure 4, where at a couple of  $\text{Mpc}^{-1}$  the emission for the diffuse IGM is about four magnitudes smaller than the galactic emission, together with the CCC in Figure 7 (right) being two magnitudes higher for the diffuse IGM, this translates to a similar power for the dimensional cross-power spectrum of the diffuse IGM versus galactic emission at a couple of  $\text{Mpc}^{-1}$  in the left panel of Figure 7, when comparing with equation (18). The scattered IGM displays a turn-over from negative cross-correlation at small  $k$  (large scales) to positive cross-correlation at larger  $k$  (small scales) that is shifted to larger scales with respect to the turn-over for galactic emission, as one can anticipate already from the extension of emitting regions for different Lyman- $\alpha$  components in the simulation boxes shown above.

Also for lower redshift a smaller negative CCC for the turn-over from negative to positive cross-correlation at  $k \approx 4-5 \text{ Mpc}^{-1}$ , together with stronger anti-correlation at large scales, can be observed in our model, meaning the ionized bubbles extend to larger scales more frequently throughout the IGM when the universe is more ionized. The turn-over scale around a few  $\text{Mpc}^{-1}$  is somewhat sensitive to reionization history, as it hints to

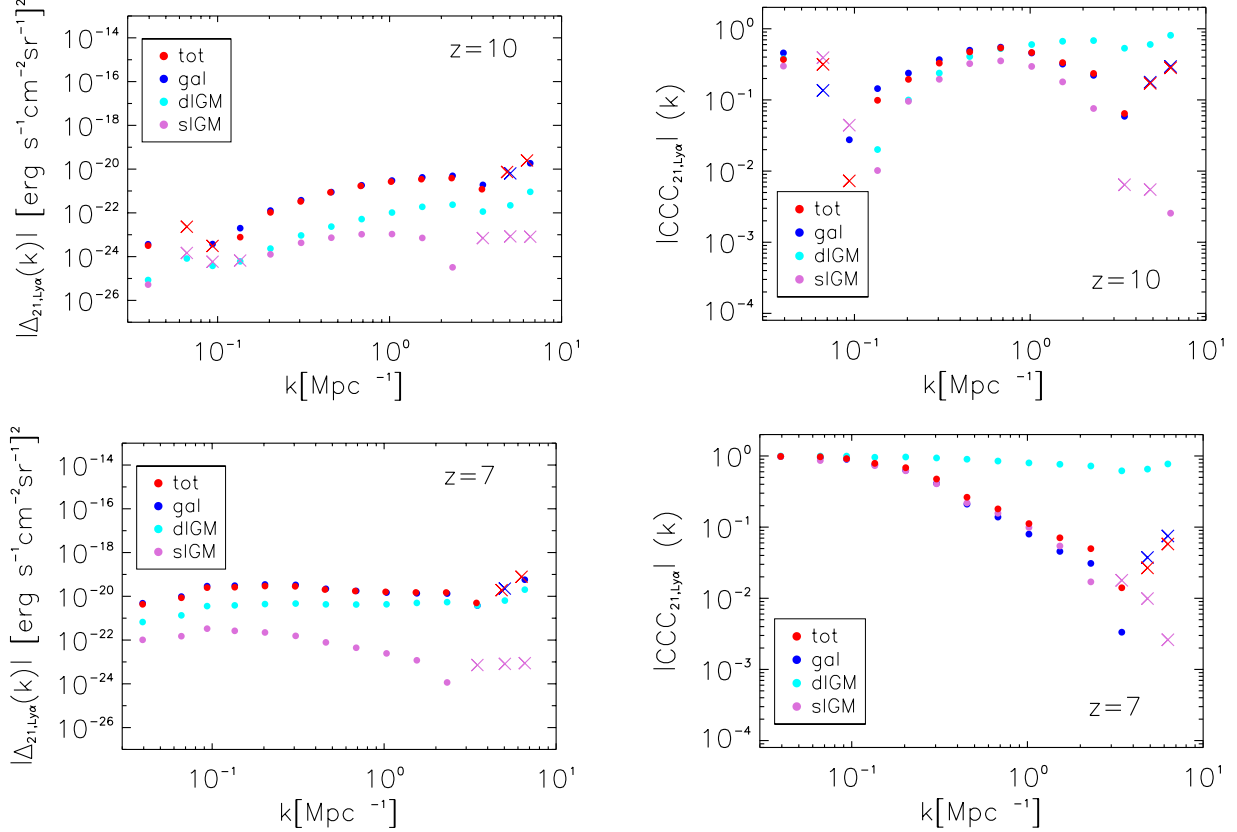


**Figure 7.** Dimensional cross-power spectra (left) and cross-correlation coefficient CCC (right) of 21 cm fluctuations and total Ly $\alpha$  brightness fluctuations (tot, red), as well as three components of Ly $\alpha$  emission, being galactic (gal, blue) and both diffuse IGM (dIGM, cyan) as well as scattered IGM (sIGM, orchid) at  $z = 10$ ,  $x_{\text{HI}} = 0.87$  (top panels) and  $z = 7$ ,  $x_{\text{HI}} = 0.27$  (bottom panels); depicted is the absolute value, crosses denote positive, points negative cross-correlation.

the typical size of the smallest ionized regions resolved, whereas the morphology of the cross-correlation shows a clear dependence on reionization model parameters like the ionizing photon mean free path  $R_{\text{mfp}}^{\text{UV}}$ , see for example Figure 9 in the following section. We leave the exact parameter dependence for the shift of the turn-over scale for future studies, keeping the overall reionization history fixed throughout this study, except for a brief peek in Section 3.1.2.

When comparing with other work, for example Lidz et al. (2009) noted, that the cross-power spectrum with Lyman- $\alpha$  emitters turns positive on small scales around  $1 \text{ Mpc}^{-1}$ . When the minimum detectable galaxy host mass is below the minimum host mass for ionizing sources, then a changed minimum detectable host mass leads to a shift in the turnover scale. For the relation between luminosity and halo mass chosen here, this shift seems to be negligible. Further studies with varied minimum host masses for galaxies and for ionizing sources, preferably at higher resolution, might be advisable. Also in Sobacchi et al. (2016) a similar turn-over seems possible above  $\approx 1 \text{ Mpc}^{-1}$  when cross-correlating 21 cm fluctuations with Ly $\alpha$  emitters. And Silva et al.

(2013) find a turn-over at high  $k$ , here at scales of the order of  $\approx 10 \text{ h Mpc}^{-1}$ , when neglecting IGM emission and assuming Ly $\alpha$  to be a biased tracer of the dark matter field, calculating the Ly $\alpha$ -galaxy/21 cm cross-correlation via cross-correlation power spectra between the ionized field and matter density fluctuations, and the matter power spectra themselves. This work suggests that when the fraction of ionized hydrogen becomes higher at lower redshift, the turn-over scale is shifted to larger scales. Given differences in modelling and approximations made, for example when defining ionized regions themselves, a decently similar behaviour with scale is encouraging for future modelling efforts.

In Figure 8 we illustrate the change of the dimensional cross-power spectra (left panels) and the cross-correlation coefficient (right panels) for the diffuse IGM component of Ly $\alpha$  emission at redshift  $z = 10$  (top panels) and  $z = 7$  (bottom panels), when neglecting fluctuations in gas temperature  $T_K$  and comoving baryonic density  $n_b$ , versus taking them into account, as discussed for simulation boxes and power spectra in Section 2.2.4. The cross-correlation for constant gas temperature and comoving baryonic density sets a lower limit for the



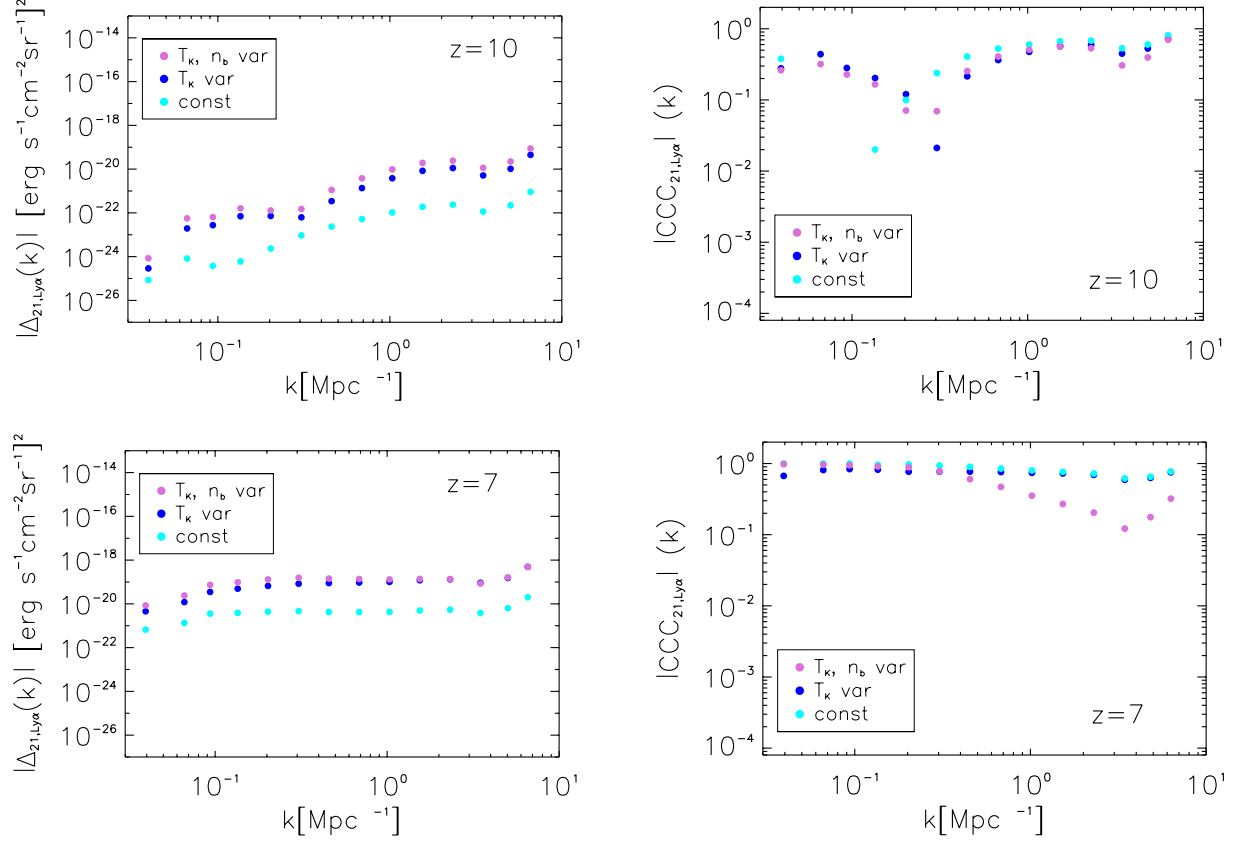


**Figure 8.** Dimensional cross-power spectra (left) and cross-correlation coefficient CCC (right) of 21 cm fluctuations and the diffuse IGM component of Ly $\alpha$  emission: taking into account fluctuations in both gas temperature  $T_K$  and comoving baryonic density  $n_b$  (orchid), only fluctuations in gas temperature  $T_K$  (blue), and for constant  $T_K$  and  $n_b$ , at  $z = 10$ ,  $x_{HI} = 0.87$  (top panels) and  $z = 7$ ,  $x_{HI} = 0.27$  (bottom panels); depicted is the absolute value, points denote negative cross-correlation.

cross-correlation signal of diffuse IGM emission in Ly $\alpha$ . The characteristic shape is similar in all three cases depicted for redshift  $z = 10$  and  $z = 7$ .

### 3.1.2. Some parameter studies

Here we show the impact of varying selected model parameters on the cross-correlation signal between 21 cm and Ly $\alpha$  brightness fluctuations. Parameters we vary, while keeping the overall reionization history fixed, are the duty cycle  $f_{duty}$ , which determines the halo occupying fraction for Ly $\alpha$  emitting galaxies as introduced in Section 2.2.4, and the escape fraction  $f_{esc}$  of Ly $\alpha$  photons from Ly $\alpha$  emitting galaxies. As an example we also vary the mean free path of ionizing radiation  $R_{mfp}^{UV}$ , which will affect the reionization history. We note, that also the variation of parameters like the escape fraction  $f_{esc}$  will alter the reionization history, when, instead of the usual ionizing efficiency  $\zeta$  as an effective parameter for the amount of ionizing radiation released, the equilibrium between ionizing and recombination rate is used to define ionized regions, as was done in Silva et al. (2013). Studying the impact on the cross-correlation of the definition applied for ionized regions might be an interesting future avenue.

In Figure 9 the cross-correlation coefficient (CCC) for a mean free path of ionizing radiation  $R_{mfp} = 40$  Mpc and  $R_{mfp} = 3$  Mpc is compared. At redshift  $z = 10$ , the CCC shows a very similar behaviour with mean sizes of ionized regions of  $\approx 1.5$  Mpc for both models, marked by a black dot and triangle. Until redshift  $z = 7$  both models differ more strongly, and the case of a higher mean free path  $R_{mfp} = 40$  Mpc displays a lower neutral fraction of  $\bar{x}_{HI} = 0.27$  as well as larger ionized regions of  $\approx 12.8$  Mpc on average, as opposed to  $\bar{x}_{HI} = 0.37$  and average sizes of  $\approx 6.5$  Mpc for  $R_{mfp} = 3$  Mpc, rendering models with different reionization parameters distinguishable. Also the variation of ionizing efficiency  $\zeta$  and virial temperature  $T_{vir}$  will have the effect of altering the reionization history.

Regarding parameter variations we keep the reionization history fixed for, Figure 10 shows the cross-correlation coefficient for two assumed duty cycles  $f_{duty} = 1$  and  $f_{duty} = 0.05$  at redshift  $z = 10$  and  $z = 7$  and tests the impact it has on the cross-correlation signal to reduce the fraction of halos occupied with Ly $\alpha$  emitting galaxies; where halos above a minimum mass  $M_{min}$  that corresponds to a virial temperature of  $T_{vir} = 10^4$  K

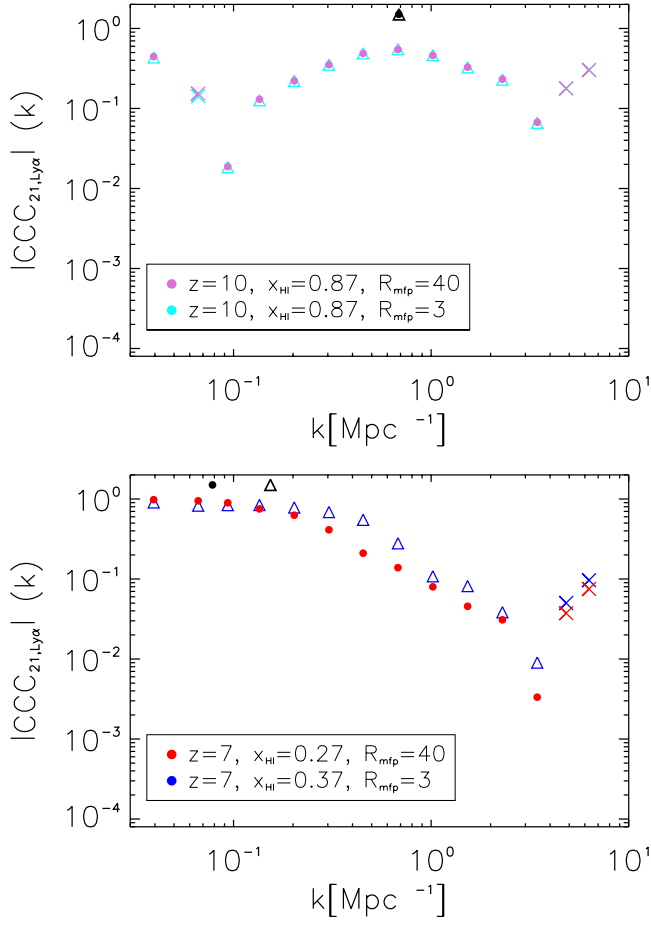


**Figure 9.** Cross-correlation coefficient CCC of 21 cm and galactic contribution to Ly $\alpha$  fluctuations for mean free path of ionizing radiation  $R_{mfp} = 40$  Mpc with  $\bar{x}_{HI} = 0.27$  (points) and  $R_{mfp} = 3$  Mpc with  $\bar{x}_{HI} = 0.37$  (triangles) at redshift  $z = 10$  (top) and  $z = 7$  (bottom); depicted is the absolute value, points denote negative CCC, crosses positive CCC; black point and triangle denote the mean size of ionized regions for  $R_{mfp} = 40$  Mpc and  $R_{mfp} = 3$  Mpc, respectively, when tracing through the simulation box along the z-axis line-of-sight.

were randomly populated. As expected, a reduction of the fraction of halos that host a Ly $\alpha$  emitting galaxy also reduces our cross-correlation signal in power. We also test the impact of varying the Ly $\alpha$  escape fraction  $f_{esc}$  in Figure 11 for redshift  $z = 10$  (top panel) and  $z = 7$  (bottom panel). The two cases of increasing and decreasing the escape fraction by 30% are shown together with the fiducial case that follows Razoumov & Sommer-Larsen (2010). Increasing the escape fraction  $f_{esc}$  has a slight tendency to decrease the cross-correlation signal at some scales, while decreasing  $f_{esc}$  can slightly increase the signal. It needs to be noted again though, that both varying  $f_{duty}$  and  $f_{esc}$  will have an effect on the reionization history, when defining ionized regions not via mean collapse fraction, but via radiation equilibrium within the ionized regions.

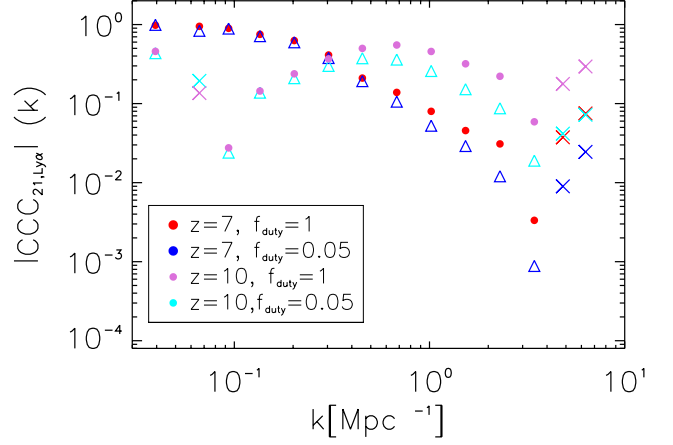


**Figure 10.** Cross-correlation coefficient CCC of 21 cm and galactic Ly $\alpha$  fluctuations for duty cycles  $f_{duty} = 1$  and  $f_{duty} = 0.05$ ; depicted is the absolute value, points denote negative CCC, crosses positive CCC.

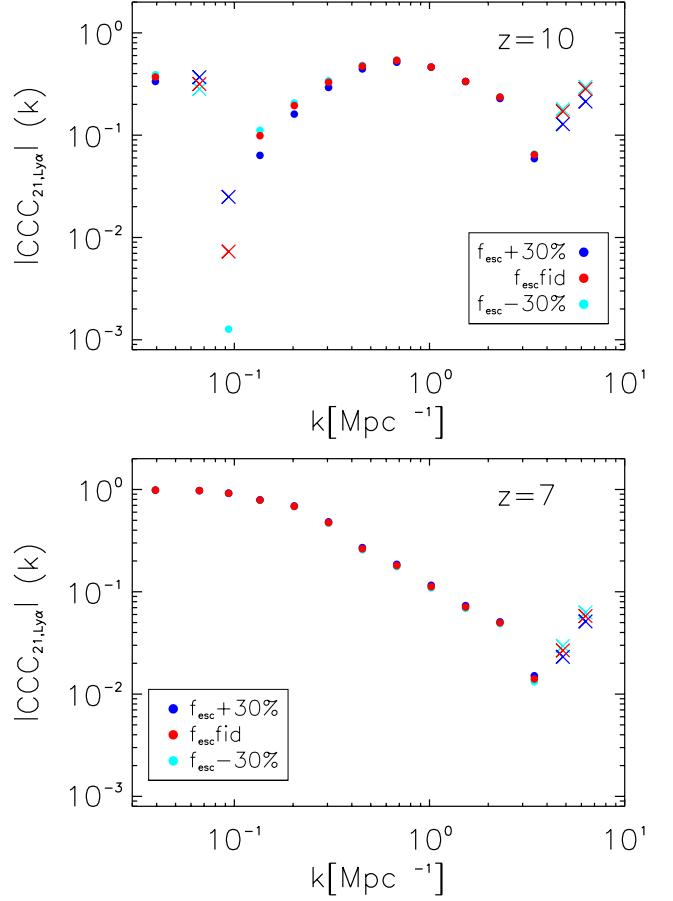


**Figure 11.** Cross-correlation coefficient CCC of 21 cm and total Ly $\alpha$  fluctuations for 30% higher and lower escape fraction  $f_{esc}$  as compared to the fiducial values from Razoumov & Sommer-Larsen (2010) at redshifts  $z = 10$  (top) and  $z = 7$  (bottom); depicted is the absolute value, points denote negative CCC, crosses positive CCC.



To sum up, the cross-correlation signal of 21 cm and Ly $\alpha$  fluctuations during the epoch of reionization is sensitive to parameters that change the reionization history or the clustering properties of emitting galaxies.

### 3.2. Ly $\alpha$ damping tail

In order to more realistically simulate the observed galactic Ly $\alpha$  emission, IGM attenuation due to the damping tail of Ly $\alpha$  needs to be taken into account. We relate the intrinsic luminosity in Ly $\alpha$  assigned to halos as in equation (9) to the observed luminosity via optical depth  $\tau_{Ly\alpha}$  for Ly $\alpha$ . This gives for the observed galactic Ly $\alpha$  luminosity

$$L_{obs}^{gal} = L^{gal} e^{-\tau_{Ly\alpha}}. \quad (19)$$

The optical depth at Ly $\alpha$  line resonance in neutral hydrogen, which makes up the not yet ionized part of the IGM, can under the assumption of uniform gas distribution be approximated at high redshift by (Gunn & Peterson 1965; Barkana & Loeb 2001)

$$\tau_s \approx 6.45 \times 10^5 \bar{x}_{HI} \left( \frac{\Omega_b h}{0.03} \right) \left( \frac{\Omega_m}{0.3} \right)^{-0.5} \left( \frac{1+z_s}{10} \right)^{1.5}, \quad (20)$$

with source redshift  $z_s$ , average neutral hydrogen fraction  $\bar{x}_{HI}$ , and present-day density parameters of matter  $\Omega_m$  and of baryons  $\Omega_b$ .

The Ly $\alpha$  radiation is redshifting between the emitting source sitting in an ionized bubble and the edge of the neutral medium around the bubble, and therefore gets shifted from the line core in resonance to the line wings of lower optical depth on the way to the observer. For Ly $\alpha$  emission at source redshift  $z_s$ , which redshifts by  $z_s - z_{obs}$  before reaching the edge of the neutral IGM fully ionized at  $z_{reion}$ , Miralda-Escudé (1998) finds for the optical depth  $\tau_{Ly\alpha}$  of Ly $\alpha$  emission the analytical result

$$\begin{aligned} \tau_{Ly\alpha}(z_{obs}) = & \tau_s \left( \frac{2.02 \times 10^{-8}}{\pi} \right) \left( \frac{1+z_{obs}}{1+z_s} \right)^{1.5} \\ & \times \left[ I \left( \frac{1+z_s}{1+z_{obs}} \right) - I \left( \frac{1+z_{reion}}{1+z_{obs}} \right) \right], \end{aligned} \quad (21)$$

with the helper function  $I(x)$  defined as

$$\begin{aligned} I(x) = & \frac{x^{4.5}}{1-x} + \frac{9}{7}x^{3.5} + \frac{9}{5}x^{2.5} + 3x^{1.5} + 9x^{0.5} \\ & - 4.5 \ln \left( \frac{1+x^{0.5}}{1-x^{0.5}} \right). \end{aligned} \quad (22)$$

In order to calculate the redshift shift between source and the neutral IGM surrounding it, we need to know the size of ionized bubbles around galaxies in halos. We therefore match our halo catalogue at given redshift to sizes of corresponding ionized regions, assuming for now

each galaxy to be in the center of the halo it is assigned to. For each halo we go from assigned sizes of the ionized region to the corresponding redshift shift and therefore  $z_{obs}$  in our fiducial cosmology, and calculate  $\tau_{Ly\alpha}$  following equation (21). We use the optical depth in order to correct intrinsic luminosities and calculate observed luminosities for each halo that include Ly $\alpha$  damping following equation (19). For determining the sizes of the ionized regions surrounding each halo, we compare two approximation here. The first simple approach consists of taking the commonest filter scale as the typical size of an ionized bubble, which is similar for most halos at a given redshift and corresponds to about 4 Mpc at  $z = 10$ , and about 20 Mpc at  $z = 7$  for our fiducial model. In the second more accurate approach we trace through our simulation box along a line-of-sight, chosen to be from each halo center along the z-axis here, until we cross the phase transition from ionized to neutral. Mean sizes of ionized regions are  $\approx 1.5$  Mpc at  $z = 10$  and  $\approx 12.8$  Mpc at  $z = 7$ , therefore about a factor of two smaller than in our first simple approach, leading to a generally stronger damping effect. In Figure 12 we show alongside with the uncorrected dimensional power spectra (top), cross-power spectra (middle) and cross-correlation coefficient (bottom) for redshift  $z = 10$  and  $z = 7$  the corrected power spectra for galactic emission in Ly $\alpha$ , left panels for the first simple approach of assuming commonest filter scale as the typical size of an ionized bubble, right panels for sizes of ionized bubbles via tracing through the simulation. As at a given redshift the typical bubble sizes are fairly similar, we observe a rather uniform decrease in power with scale, with a stronger decrease for high  $k$  in the case of tracing ionized region sizes. Also, at higher redshift the ionized bubbles are significantly smaller, the redshifting away from the line core until the bubble edge is smaller, and therefore the damping effect is bigger (up to two orders of magnitude) at redshift  $z = 10$  as compared to  $z = 7$ , where the effect is at the level of 10 to 20% for taking the commonest filter scale and at the level of  $\approx 60\%$  for tracing along the line-of-sight. For the cross-correlation power spectra (middle panels), as well as the cross-correlation coefficient (bottom panels), taking into account Ly $\alpha$  damping especially lowers the power in the more accurate approach of tracing the ionized regions in the simulation.

### 3.3. Cross-correlation of Ly $\alpha$ and H $\alpha$

Different line fluctuations trace galactic and intergalactic emission in differing ways. For example H $\alpha$  fluctuations only stem from galactic emission, whereas Ly $\alpha$  fluctuations stem both from galactic emission, plus a contribution from the IGM. We therefore cross-correlate H $\alpha$  and Ly $\alpha$  fluctuations in order to pick up

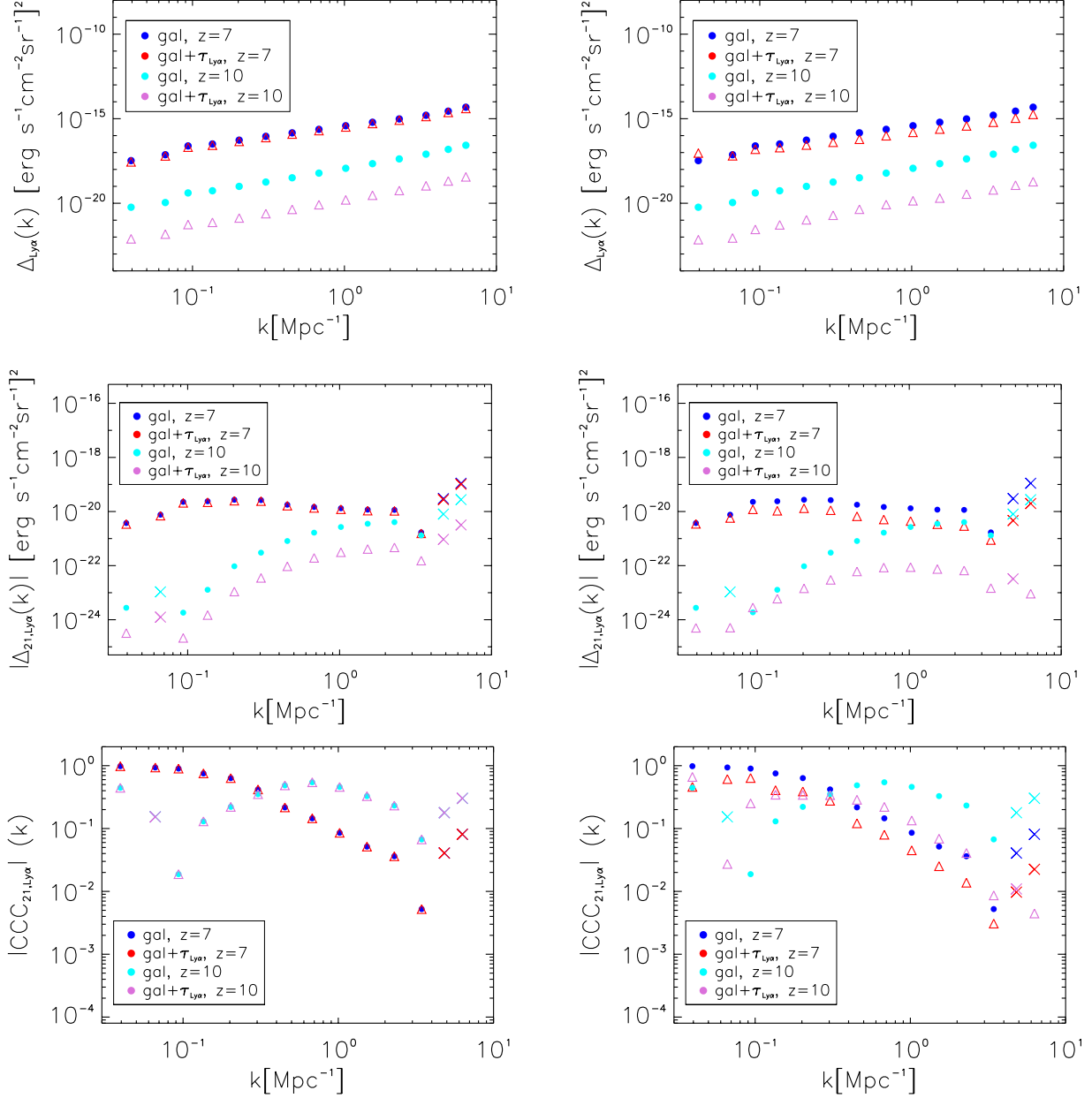


**Figure 12.** Left panels: Dimensional Ly $\alpha$  power spectra (top), dimensional cross-power spectra (middle) and cross-correlation coefficient  $CCC_{21,Ly\alpha}$  (bottom) for the galactic contribution to the Ly $\alpha$  emission with (triangles) and without (points) Ly $\alpha$  damping at redshift  $z = 10$  (cyan, orchid) and  $z = 7$  (blue, red), assuming commonest filter scale as the typical size of an ionized region. Right panels: Same as left panels, but Ly $\alpha$  damping calculated for tracing of ionized regions through the simulation along the  $z$ -axis line-of-sight. Depicted is the absolute value, points and triangles denote negative and crosses positive cross-correlation.

the IGM contribution of Ly $\alpha$  emission from the total Ly $\alpha$  emission. The resulting cross-correlation coefficient is shown in Figure 13; it is defined as  $CCC_{Ha,Ly\alpha} = \Delta_{Ha,Ly\alpha} / \sqrt{\Delta_{Ha}\Delta_{Ly\alpha}}$  (see equation (18)) and is equal to one if the two variables are perfectly correlated with each other.

When cross-correlating H $\alpha$  emission with total Ly $\alpha$  emission, “Ly $\alpha$ -tot” in both panels of Figure 13, the cross-correlation coefficient is close to one both at redshift  $z = 10$  and  $z = 7$ , with a slight decrease to-

wards higher  $k$ . When cross-correlating H $\alpha$  emission with both the diffuse (top panel) and the scattered (bottom panel) IGM component of Ly $\alpha$  emission, the cross-correlation coefficient sharply decreases towards smaller scales (higher  $k$ ). There even is a turn-over from positive cross-correlation at lower  $k$  to negative cross-correlation at high  $k$ , both at redshift  $z = 10$  and  $z = 7$ , with negative cross-correlation marked by crosses. The most prominent decrease of the cross-correlation coefficient with  $k$  is visible for the diffuse IGM at redshift  $z = 7$  (top

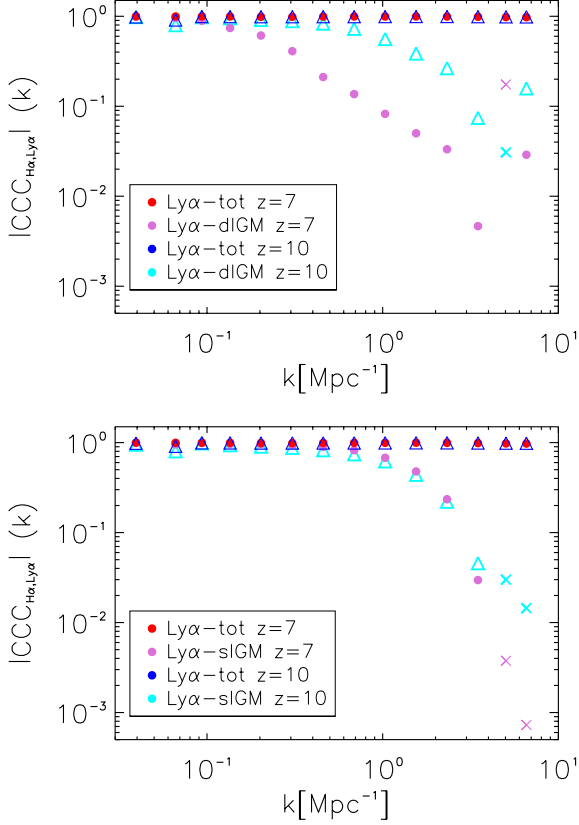


**Figure 13.**  $H\alpha$  to  $Ly\alpha$  cross-correlation coefficient  $CCC_{H\alpha, Ly\alpha}$  of brightness fluctuations at redshift  $z = 10$  and  $z = 7$ . Shown is the cross-correlation with total  $Ly\alpha$  fluctuations “ $Ly\alpha$ -tot” and with the diffuse IGM contribution “ $Ly\alpha$ -dIGM” (top), as well as the scattered IGM contribution “ $Ly\alpha$ -sIGM” (bottom); depicted is the absolute value, points and triangles denote now positive CCC, whereas crosses denote negative CCC.

panel, orchid dots). Interestingly, the redshift behaviour of the cross-correlation coefficient for diffuse IGM versus scattered IGM is different.

The different redshift behaviour for components of  $Ly\alpha$  emission when cross-correlated with  $H\alpha$  emission tracing galactic emission only, as was shown in this section, can be used to single out the IGM contribution to the total  $Ly\alpha$  emission and distinguish galactic and IGM components of  $Ly\alpha$  emission.

#### 4. SIGNAL-TO-NOISE CALCULATION

Now that we have simulated 21 cm and  $Ly\alpha$  emission in order to calculate their respective auto and cross power spectra, as well as investigated parameter effects, we turn to estimating the detectability of these spectra by future probes of the Epoch of Reionization (EoR). We first discuss the 21 cm and  $Ly\alpha$  noise auto spectra, and then their noise cross-power spectra in the following sections.

##### 4.1. 21 cm noise auto spectrum and foreground wedge

In this section we show the noise power spectrum of 21 cm emission, with our signal-to-noise calculation including cosmic variance, as well as thermal and instrumental noise. We proceed to integrate the so-called 21 cm foreground wedge in our signal-to-noise calculations. Instrument specifications are taken to match the Square Kilometre Array (SKA) stage 1 (Pritchard et al. 2015) for line intensity mapping of the 21 cm brightness temperature during the EoR.

The variance for a (dimensional) 21 cm power spectrum estimate for mode  $k$  and angle  $\mu$  between the line of sight and  $k$  (McQuinn et al. 2006a; Lidz et al. 2008), when neglecting systematic effects such as imperfect foreground removal, reads

$$\sigma_{21}^2(k, \mu) = \left[ P_{21}(k, \mu) + \frac{T_{sys}^2 V_{sur}}{B t_{int} n(k_{\perp})} W_{21}(k, \mu) \right], \quad (23)$$

where the first term is due to cosmic variance, the second term describes thermal noise of the instrument, and the window function  $W_{21}(k, \mu)$  includes the limited spectral and spatial instrumental resolution. As we want to consider SKA stage 1, we take for the survey bandwidth  $B = 8$  MHz, a total observing time of  $t_{int} = 1000$  hrs, an instrument system temperature  $T_{sys} = 400$  K, as well as an effective survey volume of  $V_{sur} = \chi^2 \Delta\chi \left( \lambda_{21}(z)^2 / A_e \right)^2$ , with redshifted 21 cm wavelength  $\lambda_{21}(z)$ , effective area per antenna  $A_e = 925 \text{ m}^2$  ( $z = 8$ ), and comoving distance and survey depth  $\chi$  and  $\Delta\chi$ . The antenna distribution enters via number density of baselines  $n(k_{\perp}) = 0.8$  that observe transverse wavenumber  $k_{\perp}$  (McQuinn et al. 2006b). The window function  $W_{21}(k, \mu)$  reads, as in Lidz et al. (2011),

$$W_{21}(k, \mu) = e^{(k_{\parallel}/k_{\parallel, res})^2 + (k_{\perp}/k_{\perp, res})^2}, \quad (24)$$

with parallel modes  $k_{\parallel} = \mu k$  along the line of sight and perpendicular modes  $k_{\perp} = (1 - \mu^2)^{1/2} k$ . The spectral and spatial instrumental resolution in parallel and perpendicular modes is given by

$$k_{\parallel, res} = \frac{2\pi R_{res} H(z)}{c(1+z)} \quad (25)$$

and

$$k_{\perp, res} = \frac{2\pi}{\chi(z) \theta_{min}}, \quad (26)$$

with comoving distance  $\chi(z)$  and angular beam (or spatial pixel) size in radians  $\theta_{min} = (x_{pix}/60)(\pi/180)$ . The instrumental resolution for a radio telescope is determined by  $R_{res} = \nu_{21}(z)/\nu_{res}$ , with frequency resolution  $\nu_{res} = 3.9 \times 10^3 \text{ Hz}$  for a SKA stage 1 type survey, and angular resolution  $x_{pix} = (\lambda_{21}(z)/l_{max})(\pi/180)/60$ , with maximum baseline  $l_{max} = 10^5 \text{ cm}$ . For example at redshift  $z = 7$  we have  $k_{\parallel, res}(z = 7) \approx 100$



and  $k_{\perp, res}(z=7) \approx 1500$ . The total variance  $\sigma^2(k)$  for the full spherically averaged power spectrum is the binned sum over all angles  $\mu$ , or equivalently all modes  $k^2 = k_{\parallel}^2 + k_{\perp}^2$ , divided by the respective number of modes per bin; it is given by

$$\frac{1}{\sigma^2(k)} = \sum_{\mu} \frac{N_m}{\sigma^2(k, \mu)}, \quad (27)$$

with number of modes  $N_m = \Delta k \Delta \mu k^2 V_{sur} / (4\pi^2)$  for binning logarithmically in  $k$ , survey volume  $V_{sur}$ , and mode as well as angle bin sizes  $\Delta k$  and  $\Delta \mu$ . We counted in our signal-to-noise calculation the number of modes  $N_m$  explicitly in each bin. The sum over angles  $\mu$  is restricted by minimal and maximal allowed values  $\mu_{min}^2 = \max(0, 1 - k_{\perp, max}^2/k^2)$  and  $\mu_{max} = \min(1, k/k_{\parallel, min})$  (McQuinn et al. 2006a) that are determined by minimum mode  $k_{\parallel, min} = 2\pi/r_{pix}$  due to survey depth and maximum mode  $k_{\perp, max} = k_{\perp, res}$  spatially resolvable by the survey.

Besides thermal and instrumental noise, as well as cosmic variance, we want to incorporate in our signal-to-noise calculation the so-called 21 cm foreground wedge, in order to restrict ourselves to a EoR window where foreground model errors do not contaminate the signal. This 21 cm foreground wedge stems from a combination of foregrounds and instrument systematics due to leakage in the 21 cm radio window. By subtraction of the foreground wedge, we mask, i.e. avoid, a significant amount of foreground. The wedge is defined for the cylindrically averaged 2D power spectrum via a relation between mode  $k_{\perp}$  perpendicular and mode  $k_{\parallel}$  parallel to the line of sight. This relation reads (Morales et al. 2012; Liu et al. 2014)

$$k_{\parallel} \leq \frac{\chi(z) E(z) \theta_0}{d_H(1+z)} k_{\perp}, \quad (28)$$

with characteristic angle  $\theta_0$ , comoving distance  $\chi(z)$ , Hubble distance  $d_H$ , and Hubble function  $E(z) = H(z)/H_0$ , which determine the slope of the wedge. The most pessimistic assumption for the characteristic angle  $\theta_0$  would be to include contamination from sources on the horizon, i.e.,  $\theta_0 = \pi/2$ . But contaminations from residual sources are band limited by the instrument field-of-view, so that it is possible to avoid contamination from sources outside the primary beam, which would make the EoR window significantly larger (Pober et al. 2014; Jensen et al. 2016) and  $\theta_0$  significantly smaller, of the order of 10 degrees. Figure 14 shows the cylindrically averaged 21 cm power spectrum both with and without foreground wedge subtraction for a survey with characteristic angle  $\theta_0 \approx 15^\circ$  for redshift  $z = 10$  (top panels) and  $z = 7$  (bottom panels). The same characteristic angle was used for the 21 cm spher-

ically averaged noise power spectrum with foreground avoidance shown in Figure 15 (right panel). The subtraction of the foreground wedge leads to loss in power and signal-to-noise for larger  $k$ -modes as compared to the 21 cm noise power spectrum without the wedge removed (left panel); in both panels error bars account for cosmic noise, thermal noise and instrumental resolution. Encouragingly the loss in power for the spherically averaged power spectrum is restricted to higher  $k$ -modes and a reconstruction of the full power spectrum from data might be possible. As we can see here, the detection of the power spectrum of 21 cm fluctuations over around two decades in spatial scale is feasible with future 21 cm experiments, making the detection range of the Ly $\alpha$  power spectrum the limiting factor for the cross-correlation of 21 cm and Ly $\alpha$  fluctuations.

#### 4.2. Ly $\alpha$ noise auto spectrum

Here we show the noise power spectrum of total Ly $\alpha$  emission, comprised of galactic, diffuse and scattered IGM contributions. In the signal-to-noise calculation we include cosmic variance, as well as thermal and instrumental noise, while taking also Ly $\alpha$  damping into account (see Section 3.2). In the following we use instrument specifications of the proposed all-sky near-infrared survey satellite SPHEREx (Doré et al. 2014) for line intensity mapping at high redshifts, as summarized in Table 3. For the thermal noise variance we take  $\sigma_N \approx 3 \text{ kJy sr}^{-1}$ , corresponding to  $\sigma_N \approx 3 \times 10^{-20} \text{ erg s}^{-1} \text{ cm}^{-2} \text{ Hz}^{-1} \text{ sr}^{-1}$ , which is consistent with sensitivity at 5 $\sigma$  given in Doré et al. (2016) of 18–19 in AB magnitude for relevant bands<sup>2</sup>. Assuming a pure white-noise spectrum the thermal noise power spectrum reads

$$P_{N, Ly\alpha} = \sigma_N^2 V_{vox}. \quad (29)$$

The comoving pixel volume corresponds to  $V_{vox} = A_{pix} r_{pix} \approx 0.3 \text{ Mpc}^3$ , product of pixel area  $A_{pix} = 6.2'' \times 6.2''$  in comoving Mpc and comoving pixel depth  $r_{pix} = \chi(R_{res})$ , which corresponds to the comoving length at frequency resolution  $R_{res}$ . The frequency resolution is  $R_{res} = 41.5$  in the 0.75–4.1  $\mu\text{m}$  range of interest for Ly $\alpha$  emission during reionization. The variance, as a function of  $k$ -mode and angle  $\mu$  between line of sight and mode  $k$ , reads

$$\sigma_{Ly\alpha}^2(k, \mu) = [P_{Ly\alpha}(k, \mu) + \sigma_N^2 V_{vox} W_{Ly\alpha}(k, \mu)]. \quad (30)$$

The first term is due to cosmic variance,  $\sigma_N$  includes thermal noise and the window function  $W_{Ly\alpha}(k, \mu)$  accounts for limited spatial and spectral instrumental res-

<sup>2</sup> magnitude to flux density converter:  
http://ssc.spitzer.caltech.edu/warmmission/propkit/pet/magtojy/

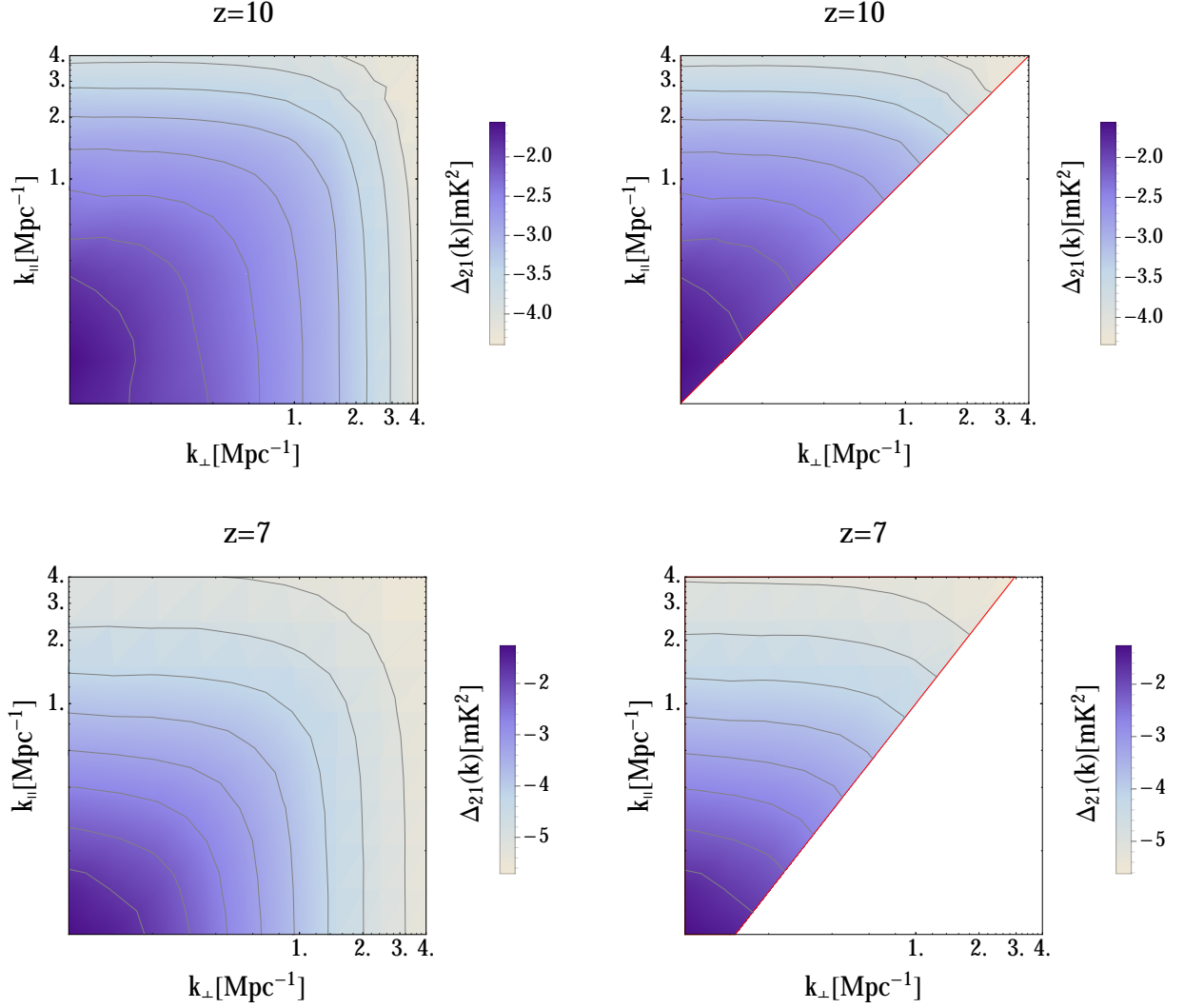


**Figure 14.** Cylindrically averaged 21 cm power spectra at  $z = 10$ ,  $\bar{x}_{\text{HI}} = 0.87$  (top) and  $z = 7$ ,  $\bar{x}_{\text{HI}} = 0.27$  (bottom). Left: No foreground removal, full power spectra extracted from the simulation boxes with 200Mpc box length as shown in Figure 1 (middle). Right: Cylindrically averaged 21 cm power spectra where the foreground wedge defined in Equation (28) for survey characteristic angle  $\theta_0 \approx 15^\circ$  is removed.

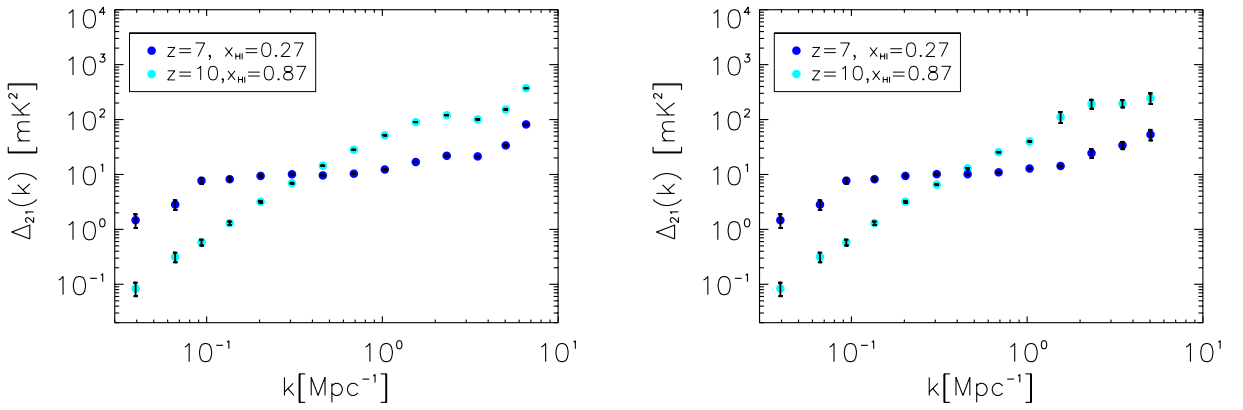


**Figure 15.** Left: 21 cm noise power spectrum (spherically averaged), including cosmic variance, thermal and instrumental noise for a SKA stage 1 type survey; Right: 21 cm noise power spectrum after removal of the foreground wedge defined in Equation (28), for survey characteristic angle  $\theta_0 = 15^\circ$ ; again including cosmic variance, thermal and instrumental noise; see Table 2 for instrument specifications; redshift  $z = 7$  and mean neutral fraction  $\bar{x}_{\text{HI}} = 0.27$  in blue,  $z = 10$  and  $\bar{x}_{\text{HI}} = 0.87$  in cyan.

**Table 2.** Instrument specifications for 21 cm survey: SKA stage 1

$\nu_{res}$	$l_{max}$	$T_{sys}$	$t_{int}$	B (z=8)	$A_e$ (z=8)	$n_{\perp}$
(kHz)	(cm)	(K)	(hrs)	(MHz)	(m <sup>2</sup> )	
3.9	$10^5$	400	1000	8	925	0.8

NOTE. - See Section 4.1 for details on error calculations; specifications taken from [Pritchard et al. \(2015\)](#).

**Table 3.** Instrument specifications for Ly $\alpha$  survey: SPHEREx

$x_{pix}$	$R_{res}$	$R_{res}$	$\sigma_N$	$V_{vox}$
(")	(0.75-4.1 $\mu$ m)	(4.1-4.8 $\mu$ m)	(erg s <sup>-1</sup> cm <sup>-2</sup> Hz <sup>-1</sup> sr <sup>-1</sup> )	(Mpc <sup>3</sup> )
6.2	41.5	150	$3 \times 10^{-20}$	0.3

NOTE. - See Section 4.2 for details on error calculations; specifications taken from [Doré et al. \(2014\)](#).

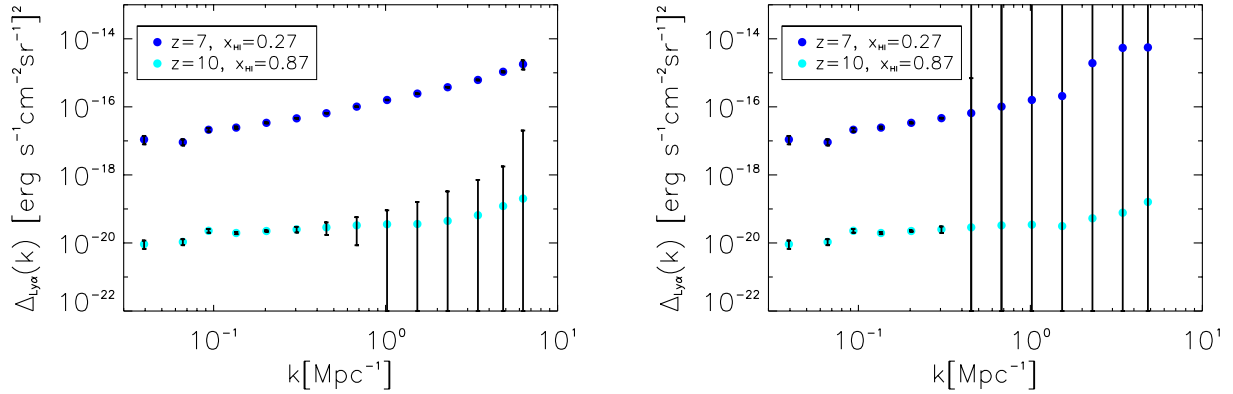


**Figure 16.** Left: Ly $\alpha$  noise power spectrum for a SPHEREx type survey, including cosmic variance, thermal and instrumental noise with  $k_{\parallel} > 0.3$  cut (for the choice of this cut see discussion in Section 4.2 and B); Right: Ly $\alpha$  noise power spectrum after removal of the foreground wedge defined in Equation (28) for survey characteristic angle  $\theta_0 \approx 15^\circ$ ; again including cosmic variance, thermal and instrumental noise with  $k_{\parallel} > 0.3$  cut for a SPHEREx type survey; see Table 3 for instrument specifications; redshift  $z = 7$  and neutral fraction  $x_{HI} = 0.27$  in blue,  $z = 10$  and  $x_{HI} = 0.87$  in cyan; all power spectra include Ly $\alpha$  damping for tracing of ionized regions through the simulation along the z-axis line-of-sight.



olution and is defined analogous to equation (24). For example at redshift  $z = 7$  equation (25) and (26) give an angular resolution of  $k_{\parallel, res}(z = 7) \approx 0.1$  and a spectral resolution of  $k_{\perp, res}(z = 7) \approx 23.7$  for the characteristics of the SPHEREx satellite. The total variance  $\sigma_{Ly\alpha}^2(k)$  for the full spherically averaged power spectrum again is the sum over the upper-half plane of angles  $\mu$ , or equivalently k-modes with  $k^2 = k_{\parallel}^2 + k_{\perp}^2$ , divided by the respective number of modes per bin defined in equation (27). We explicitly counted the number of modes  $N_m$  in each bin.

Figure 16 shows the noise power spectrum of Ly $\alpha$  fluctuations at  $z = 10$  (cyan) and  $z = 7$  (blue). The error bars account for cosmic noise and thermal noise, as well as instrumental noise. A cut in parallel modes of  $k_{\parallel} > 0.3$  was applied, as for a SPHEREx-like experiment the instrumental noise in parallel modes, i.e., the limitation due to spectral resolution, dominates over the signal at higher modes. As shown in Appendix B, this cut roughly corresponds to the k-mode, where the signal-to-noise drops below 1. Of course this presents a trade-off between a loss of power and gain of precision for the measurement via perpendicular modes left at higher k. A high significance Ly $\alpha$  power spectrum measurement is possible across more than a decade in spatial scale, which is encouraging for cross-correlation studies with 21 cm emission.

#### 4.3. 21 cm - Ly $\alpha$ cross-power spectrum

We now consider the detectability of the 21 cm - Ly $\alpha$  cross-power spectrum, a signal enabling us to constrain structure and evolution of ionized regions in the IGM during the Epoch of Reionization.

For a single mode k and angle  $\mu$  the variance estimate of the cross-power spectrum reads (Furlanetto & Lidz 2007; Lidz et al. 2009)

$$\sigma_{21, Ly\alpha}^2(k, \mu) = \frac{1}{2} [P_{21, Ly\alpha}^2(k, \mu) + \sigma_{21}(k, \mu) \sigma_{Ly\alpha}(k, \mu)], \quad (31)$$

with the 21 cm - Ly $\alpha$  cross-power spectrum  $P_{21, Ly\alpha}(k, \mu)$ , and the variance of the 21 cm and Ly $\alpha$  auto spectra  $\sigma_{21}(k, \mu)$  and  $\sigma_{Ly\alpha}(k, \mu)$  that both encompass cosmic variance, instrumental and thermal noise as defined in equations (23) and (30), respectively. The variance  $\sigma_{21, Ly\alpha}^2(k)$  for the full spherically averaged power spectrum here too is the sum over the upper-half plane of angles  $\mu$ , or equivalently k-modes with  $k^2 = k_{\parallel}^2 + k_{\perp}^2$ , divided by the respective number of modes per bin, as in equation (27). Note that the 21 cm brightness temperature  $T_b$  has been converted to brightness intensity  $I_{21}$  for the cross-power spectra shown in this section, using Planck's law at observed

frequency  $\nu$  as

$$I_{21}(\nu, T_b) = \frac{2h\nu^3}{c^2} \left( e^{\frac{h_P\nu}{k_B T_b}} - 1 \right)^{-1}, \quad (32)$$

with Boltzmann constant  $k_B$  and Planck's constant  $h_P$ .

Figure 17 shows the dimensionless 21 cm - Ly $\alpha$  noise cross-power spectra at redshift  $z = 10$  and  $z = 7$  and the corresponding detectability  $S/N$ , including cosmic variance, thermal noise and instrumental resolution effects; instrument specifications of the 21 cm and Ly $\alpha$  experiments are taken as in table 2 and 3, respectively. The two top rows of panels show the result for the 21 cm - Ly $\alpha$  noise cross-power spectra when including Lyman- $\alpha$  damping assuming the commonest filter scale as the typical size of an ionized region, see Section 3.2, while to two bottom rows of panels depict the same, but the power spectra include Lyman- $\alpha$  damping for tracing of ionized regions through the simulation along the z-axis line-of-sight. Note the absence of the turn-over to positive cross-correlation at high k for the stronger Ly $\alpha$  damping when tracing through the simulation (bottom two rows), which is due to the diffuse IGM contribution gaining importance.

For both left and right panels in Figure 17 a cut of  $k_{\parallel} > 0.3 \text{ Mpc}^{-1}$  is applied to avoid the impact of limited spectral resolution in our Ly $\alpha$  experiment, as described in the previous Section 4.2 and appendix B. The right panels in addition show the impact of foreground avoidance for the 21 cm signal, where we cut the so-called foreground wedge as described in Section 4.1 for a characteristic scale of  $\theta_0 \approx 15^\circ$ . Cutting away the foreground wedge means cutting away higher perpendicular modes  $k_{\perp}$ , which together with the cut of  $k_{\parallel} > 0.3 \text{ Mpc}^{-1}$  degrades the signal at k above that scale, but leaves the shape of the cross-correlation signal mostly unaltered.

Measuring 21 cm fluctuations in the foreground window might be possible though by dedicated foreground modelling (Liu et al. 2014; Wolz et al. 2015), which improves the prospect of detecting of the 21 cm - Ly $\alpha$  cross-correlation signal at higher k. Alternatively, a higher instrumental resolution around  $R_{res} \approx 200 - 300$  and an adjustment of instrument specifications might even render the turn-over around a couple of  $\text{Mpc}^{-1}$  from negative to positive in the cross-correlation signal detectable. For the optimistic case of improved foreground avoidance, a detection of the 21 cm - Ly $\alpha$  cross-correlation signal is feasible over one to two decades in scale, depending on assumptions, and reaching a detectability above 5- $\sigma$  confidence over about a half a decade to a decade in scale. Detecting the cross-power spectrum at high redshift for use of joint analysis with power spectra themselves is therefore feasible. It is possible to measure the varying morphology of the cross-correlation signal at different redshifts, which in turn depends on the mor-

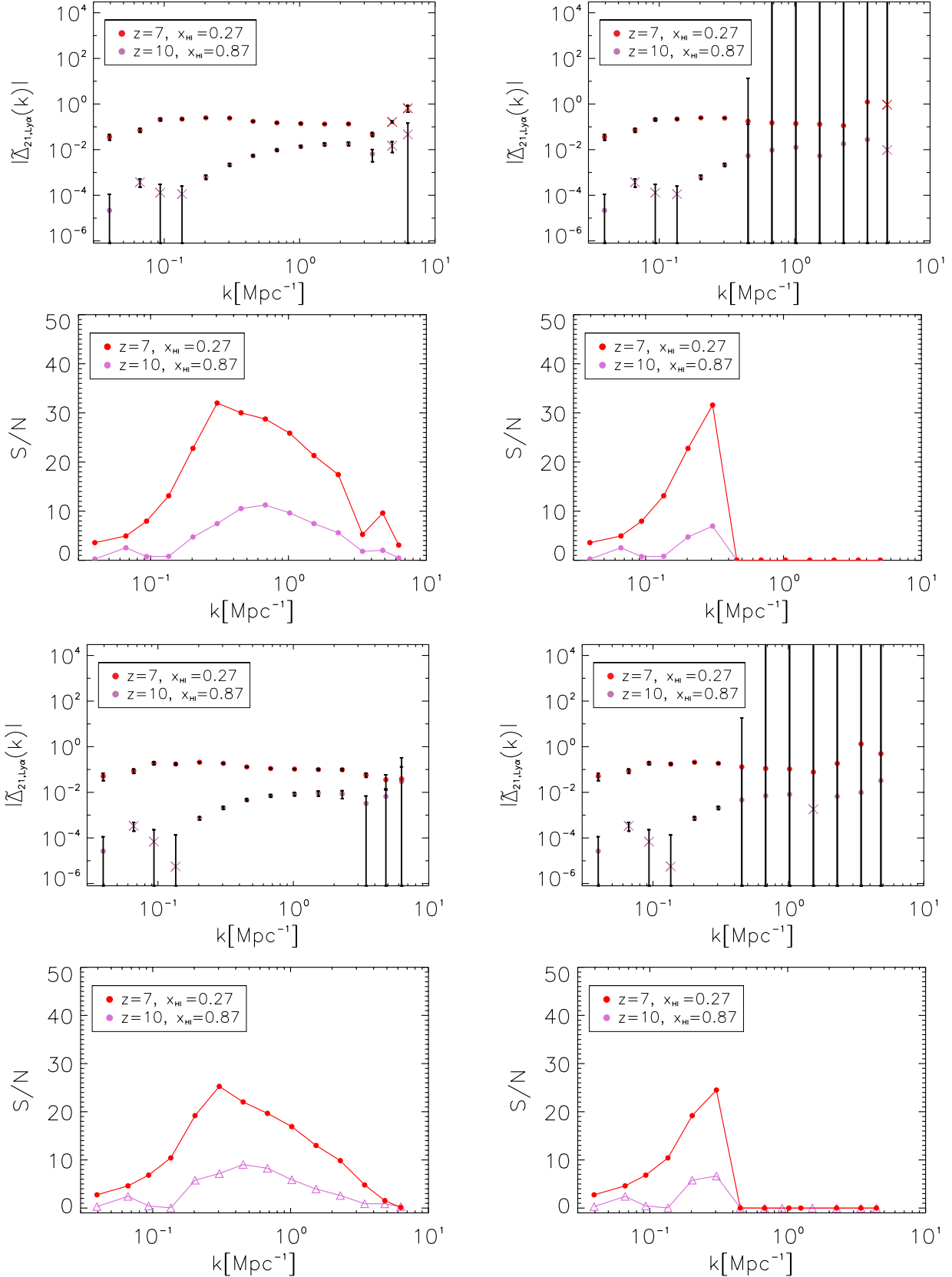


**Figure 17.** Top two rows: Dimensionless cross-correlation power spectra (CCC, top) and signal-to-noise (S/N, bottom) of 21 cm and total Ly $\alpha$  fluctuations with error calculations including cosmic variance, thermal and instrumental noise for a survey of 21 cm emission, type SKA stage 1, and a survey of Ly $\alpha$  emission, type SPHEREx, for experiment characteristics see Table 2 and 3; points denote negative and crosses positive cross-correlation; Left: Cut of  $k_{\parallel} > 0.3$  (see discussion in Section 4.2 and B); Right: Cut of  $k_{\parallel} > 0.3$  and removal of the foreground wedge defined in Equation (28) for survey characteristic angle  $\theta_0 \approx 15^\circ$ ; redshift  $z = 7$  and neutral fraction  $x_{\text{HI}} = 0.27$  in red,  $z = 10$  and  $x_{\text{HI}} = 0.87$  in orchid. All spectra include Ly $\alpha$  damping assuming commonest filter scale as the typical size of an ionized region, see Section 3.2. Bottom two rows: Same as above, but power spectra include Ly $\alpha$  damping for tracing of ionized regions through the simulation along the  $z$ -axis line-of-sight.

phology and ionization fraction of the IGM during reionization, and therefore reionization model parameters.

## 5. DISCUSSION

We demonstrate the feasibility to detect cross-power spectra with future intensity mapping probes, by simulating fluctuations in 21 cm, Ly $\alpha$  and H $\alpha$  emission. Fast and semi-numerical modelling of different tracers will be crucial when constraining the Epoch of Reionization, probing the ionized and neutral medium back to when the first galaxies started to ionize the medium around them. Making use of information beyond power spectra themselves will help to break degeneracies and constrain reionization model parameters.

We started by presenting modelling and power spectra for 21 cm emission tracing the neutral IGM, for Ly $\alpha$  galactic, diffuse IGM and scattered IGM components, as well as H $\alpha$  emission. Proceeding to the cross-power spectra between 21 cm emission and different Ly $\alpha$  components, we showed the variation of the cross-power signal with some of the model parameters, laying the ground for future parameter determinations. On top of that, the cross-power spectrum between 21 cm emission and lines other than Ly $\alpha$  can be used to extract further information on the state of the intergalactic medium, as shown for the cross-correlation with H $\alpha$  emission. Here the relative strengths of different Ly $\alpha$  emission components can be extracted from the cross-correlation signal. We show the detectability of the 21 cm and Ly $\alpha$  cross-correlation signals with future probes like SKA and SPHEREx, also when the Ly $\alpha$  damping tail and foreground avoidance are included in error calculations.

To extend this study, further parameter explorations and a refinement of foreground treatment, as well as the derivation of possible future parameter constraints involving accurate semi-numerical modelling, are a fruitful goal. Together with further adjustment of the modelling in light of high redshift data, as well as hydro-numerical simulations, this will bring us closer to extracting as much information as possible about the high-redshift Universe with upcoming intensity mapping experiments.

AC acknowledges support from NSF CAREER AST-0645427 and AST-1313319, and the NASA grants NNX16AF39G and NNX16AF38G. CF acknowledges support from NASA grants NASA NNX16AJ69G and NASA NNX16AF39G. The computational analysis was performed using the High Performance Computing HPC@UCPH, HPC facility at the University of Copenhagen.



## APPENDIX

A. COMPARISON OF  $\text{Ly}\alpha$  SPECTRA - OTHER WORK

Here we compare for consistency the  $\text{Ly}\alpha$  power spectra in surface brightness ( $\nu I_\nu$ ) obtained in this work for the galactic contribution, as well as diffuse and scattered IGM contributions, see Figure 4 in Section 2.2, with  $\text{Ly}\alpha$  power spectra from other work. Figure A1 checks against the total galactic power spectrum from [Silva et al. \(2013\)](#) (black lines, left panels), and against the theoretical power spectrum for halo emission from [Pullen et al. \(2014\)](#) (dashed and dash-dotted lines, right panels), both at redshift  $z = 10$  (top) and  $z = 7$  (bottom). Encouragingly, the power spectra roughly agree with each other, especially given the differing approaches in modelling.

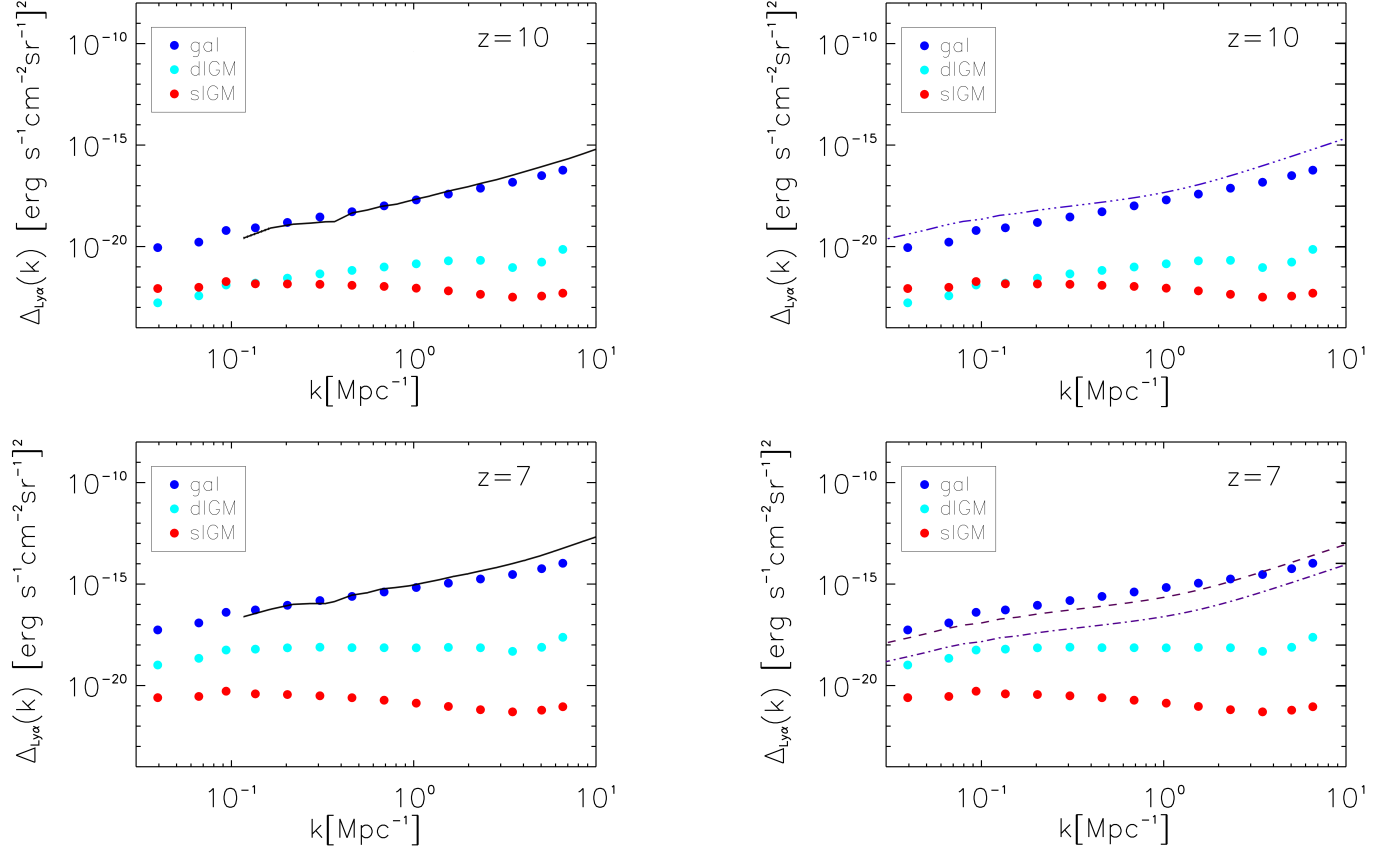


**Figure A1.** Comparison of  $\text{Ly}\alpha$  power spectra in surface brightness ( $\nu I_\nu$ ) for galactic contribution, as well as diffuse and scattered IGM contributions, see Figure 4 in Section 2.2, with spectra taken from [Silva et al. \(2013\)](#) (left, black lines) and [Pullen et al. \(2014\)](#) (right, top panel dash-dotted for  $z = 10$ , bottom panel dashed for  $z = 6$  and dash-dot for  $z = 8$ ).

### B. S/N AND MODE CUTS

For completeness we show here the Ly $\alpha$  power spectra in surface brightness ( $\nu I_\nu$ ) for redshift  $z = 10$  and  $z = 7$  in Figure B2 (left panel), including cosmic variance, thermal and instrumental noise, but before mode cuts have been applied. The sharp drop-off in signal-to-noise around  $k = 0.3 \text{ Mpc}^{-1}$  (right panel) is due to the spectral resolution limit in parallel modes for the SPHEREx satellite investigated. We therefore chose for all plots shown in Sections 4.2 and 4.3 a cut of  $k_{\parallel} < 0.3$ , around the mode where the S/N drops below 1, in order to avoid instrumental noise dominating the signal.

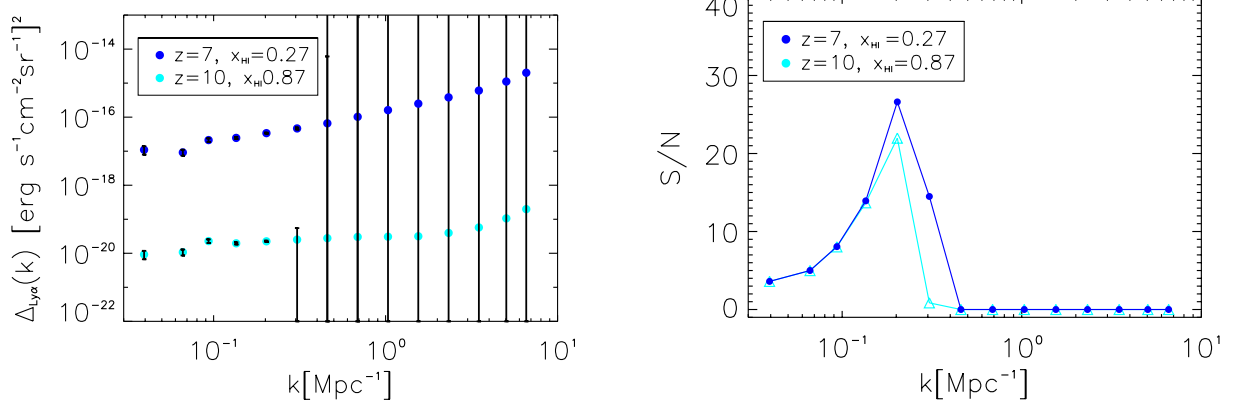


**Figure B2.** Left: Ly $\alpha$  noise power spectrum in surface brightness ( $\nu I_\nu$ ), including cosmic variance, thermal and instrumental noise for a SPHEREx type survey; Right: Corresponding detectability of the Ly $\alpha$  power spectrum, showing the total S/N, with for example a S/N of 10 indicating a detection at 10- $\sigma$  confidence; redshift  $z = 7$  and neutral fraction  $x_{\text{HI}} = 0.27$  in blue,  $z = 10$  and  $x_{\text{HI}} = 0.87$  in cyan.

## REFERENCES

- Abel, T., Anninos, P., Zhang, Y., & Norman, M. L. 1997, *New Astron.*, 2, 181
- Barkana, R., & Loeb, A. 2001, *Phys. Rept.*, 349, 125
- . 2005, *Astrophys. J.*, 626, 1
- Beardsley, A. P., Hazelton, B. J., Morales, M. F., et al. 2013, *MNRAS*, 429, L5
- Bowman, J. D., Cairns, I., Kaplan, D. L., et al. 2013, *PASA*, 30, e031
- Brocklehurst, M. 1971, *MNRAS*, 153, 471
- Comaschi, P., Yue, B., & Ferrara, A. 2016, arXiv:1605.05733
- Conroy, C., & Wechsler, R. H. 2009, *Astrophys. J.*, 696, 620
- DeBoer, D. R., Parsons, A. R., Aguirre, J. E., et al. 2016, *ArXiv e-prints*, arXiv:1606.07473
- Dopita, M. A., Groves, B. A., Sutherland, R. S., & Kewley, L. J. 2003, *Astrophys. J.*, 583, 727
- Doré, O., Bock, J., Ashby, M., et al. 2014, *ArXiv e-prints*, arXiv:1412.4872
- Doré, O., et al. 2016, arXiv:1606.07039
- Fan, X., Strauss, M. A., Becker, R. H., et al. 2006, *AJ*, 132, 117
- Fardal, M. A., Katz, N., Weinberg, D. H., Dave, R., & Hernquist, L. 2001, arXiv:astro-ph/0107290
- Fernandez, E., & Komatsu, E. 2006, *Astrophys. J.*, 646, 703
- Furlanetto, S., Oh, S. P., & Briggs, F. 2006, *Phys. Rept.*, 433, 181
- Furlanetto, S. R., & Lidz, A. 2007, *ApJ*, 660, 1030
- Gong, Y., Cooray, A., Silva, M., et al. 2012, *ApJ*, 745, 49
- Gould, A., & Weinberg, D. H. 1996, *Astrophys. J.*, 468, 462
- Gunn, J. E., & Peterson, B. A. 1965, *ApJ*, 142, 1633
- Guo, Q., White, S., Boylan-Kolchin, M., et al. 2011, *MNRAS*, 413, 101
- Hayes, M., Schaerer, D., Östlin, G., et al. 2011, *ApJ*, 730, 8
- Hummer, D. G., & Storey, P. J. 1987, *MNRAS*, 224, 801
- Hutter, A., Dayal, P., Miller, V., & Trott, C. 2016, arXiv:1605.01734
- Jensen, H., Majumdar, S., Mellema, G., et al. 2016, *Mon. Not. Roy. Astron. Soc.*, 456, 66
- Kennicutt, Jr., R. C. 1998, *Astrophys. J.*, 498, 541
- Koopmans, L., Pritchard, J., Mellema, G., et al. 2015, *Advancing Astrophysics with the Square Kilometre Array (AASKA14)*, 1
- Lidz, A., Furlanetto, S. R., Oh, S. P., et al. 2011, *ApJ*, 741, 70
- Lidz, A., Zahn, O., Furlanetto, S. R., et al. 2009, *ApJ*, 690, 252
- Lidz, A., Zahn, O., McQuinn, M., Zaldarriaga, M., & Hernquist, L. 2008, *ApJ*, 680, 962
- Liu, A., Parsons, A. R., & Trott, C. M. 2014, *PhRvD*, 90, 023018
- Liu, A., Parsons, A. R., & Trott, C. M. 2014, *Phys. Rev.*, D90, 023019
- Maraston, C. 2005, *Mon. Not. Roy. Astron. Soc.*, 362, 799
- McGreer, I. D., Mesinger, A., & D’Odorico, V. 2015, *MNRAS*, 447, 499
- McQuinn, M., Zahn, O., Zaldarriaga, M., Hernquist, L., & Furlanetto, S. R. 2006a, *ApJ*, 653, 815
- . 2006b, *ApJ*, 653, 815
- Mesinger, A., & Furlanetto, S. 2007, *ApJ*, 669, 663
- Mesinger, A., Furlanetto, S., & Cen, R. 2011, *MNRAS*, 411, 955
- Miralda-Escudé, J. 1998, *The Astrophysical Journal*, 501, 15
- Morales, M. F., Hazelton, B., Sullivan, I., & Beardsley, A. 2012, *ApJ*, 752, 137
- Ocvirk, P., Gillet, N., Shapiro, P. R., et al. 2016, *MNRAS*, arXiv:1511.00011
- Partl, A. M., Maselli, A., Ciardi, B., Ferrara, A., & Müller, V. 2011, *MNRAS*, 414, 428
- Pober, J. C., et al. 2014, *Astrophys. J.*, 782, 66
- Popesso, P., Biviano, A., Rodighiero, G., et al. 2012, *A&A*, 537, A58
- Pritchard, J., Ichiki, K., Mesinger, A., et al. 2015, *Advancing Astrophysics with the Square Kilometre Array (AASKA14)*, 12
- Pritchard, J. R., & Furlanetto, S. R. 2007, *Mon. Not. Roy. Astron. Soc.*, 376, 1680
- Pullen, A. R., Doré, O., & Bock, J. 2014, *Astrophys. J.*, 786, 111
- Razoumov, A. O., & Sommer-Larsen, J. 2010, *ApJ*, 710, 1239
- Santos, M. G., Amblard, A., Pritchard, J., et al. 2008, *Astrophys. J.*, 689, 1
- Santos, M. G., Ferramacho, L., Silva, M. B., Amblard, A., & Cooray, A. 2010, *MNRAS*, 406, 2421
- Schaerer, D. 2002, *Astron. Astrophys.*, 382, 28
- Serra, P., Dor, O., & Lagache, G. 2016, arXiv:1608.00585
- Silva, M. B., Santos, M. G., Gong, Y., Cooray, A., & Bock, J. 2013, *ApJ*, 763, 132
- Sobacchi, E., Mesinger, A., & Greig, B. 2016, arXiv:1602.04837
- Springel, V. 2005, *Mon. Not. Roy. Astron. Soc.*, 364, 1105
- Springel, V., Yoshida, N., & White, S. D. M. 2001, *New Astron.*, 6, 79
- Trac, H., Cen, R., & Loeb, A. 2008, *Astrophys. J.*, 689, L81
- van Haarlem, M. P., Wise, M. W., Gunst, A. W., et al. 2013, *A&A*, 556, A2
- Wolz, L., Abdalla, F. B., Alonso, D., et al. 2015, *PoS, AASKA14*, 035
- Zel’dovich, Y. B. 1970, *A&A*, 5, 84